Development of a propulsion technology using lunar resources

by

Ümit Yelken

A Dissertation Submitted to the
Graduate School of Sciences and Engineering
in Partial Fulfillment of the Requirements for
the Degree of

Doctor of Philosophy

in

Mechanical Engineering

KOÇ ÜNİVERSİTESİ

March 10, 2025

Development of a propulsion technology using lunar resources

Koç University

Graduate School of Sciences and Engineering

This is to certify that I have examined this copy of a doctoral dissertation by

Ümit Yelken

and have found that it is complete and satisfactory in all respects,
and that any and all revisions required by the final
examining committee have been made.

Committee Members:

_____

Assoc. Prof. Arif Karabeyoğlu

_____

Prof. Dr. Metin Muradoğlu

_____

Prof. Dr. Onur Tunçer

_____

Prof. Dr. Ibrahim Ozkol

_____

Assoc. Prof. Zeynep Parlar

Date: _____

To my family

ABSTRACT

Development of a propulsion technology using lunar resources
Ümit Yelken
Doctor of Philosophy in Mechanical Engineering
March 10, 2025

This dissertation explores the development of a hybrid rocket propulsion technology utilizing lunar resources, specifically magnesium (Mg) and aluminum (Al), for sustainable space exploration. The study addresses the challenges of in-situ resource utilization (ISRU) to minimize dependency on Earth-supplied fuels, focusing on the potential of metals found in lunar soil. Through thermochemical analysis, Mg and Al are evaluated as primary fuels due to their energetic properties and abundance on the Moon. The research involves the design, production, and testing of hybrid rocket engines using metal powders combined with sodium silicate as a binder, creating a robust fuel with favorable combustion properties.

Experimental tests were conducted on various fuel compositions to optimize the combustion characteristics and ensure high performance under lunar conditions. A specific focus is placed on the relationship between oxygen-to-fuel (O/F) ratio and the specific impulse (Isp) of the metal-based hybrid engine, achieving significant results with Mg-Al mixtures. The experimental results demonstrate that the optimal fuel composition, consisting of 75% magnesium and 20% aluminum, can sustain combustion efficiency with an Isp close to 350 seconds in a vacuum.

Additionally, the study addresses the challenges posed by metal oxide formation and its impact on combustion chamber stability. Solutions, including thermal management and fuel structuring, are presented to mitigate the risks associated with high-temperature operations. The results of this research contribute to the broader field of ISRU and have significant implications for future lunar missions, particularly in the context of NASA's Artemis program and other international lunar exploration initiatives. This work presents a scalable and sustainable propulsion system, positioning metal-based hybrid rockets as a viable solution for long-term lunar exploration and colonization.

ÖZETÇE

Ay madenleri kullanılarak bir roket itki teknolojisi geliştirilmesi

Ümit Yelken

Makine Mühendisliği, Doktora

10 Mart 2025

Bu tez, sürdürülebilir uzay keşfi için ay kaynaklarını kullanarak hibrit roket itki teknolojisinin geliştirilmesini incelemektedir. Çalışma, Dünya'dan sağlanan yakıtlara bağımlılığı en aza indirmek amacıyla, Ay toprağında bulunan magnezyum (Mg) ve aluminyumun (Al) yerinde kaynak kullanımı (ISRU) potansiyelini ele almaktadır. Termokimyasal analiz yoluyla, Ay'da bol miktarda bulunan Mg ve Al, enerjik özellikleri nedeniyle birincil yakıt olarak değerlendirilmiştir. Araştırma, sodyum silikat bağlayıcı ile metal tozlarının birleştirilmesiyle üretilen sağlam bir yakıtın, uygun yanma özelliklerine sahip hibrit roket motorlarının tasarımını, üretimini ve test edilmesini kapsamaktadır. Çeşitli yakıt bileşimleri üzerinde gerçekleştirilen deneysel testlerle yanma özellikleri optimize edilmiştir ve Ay koşullarında yüksek performans sağlanmıştır. Metal bazlı hibrit motorun oksijen-yakıt (O/F) oranı ile özgül itme (Isp) arasındaki ilişkiye odaklanılmış ve Mg-Al karışımlarıyla önemli sonuçlar elde edilmiştir. Deneysel sonuçlar, %75 magnezyum ve %20 alüminyum içeren optimum yakıt bileşiminin vakumda yaklaşık 350 saniyelik bir Isp ile yanma verimliliğini sürdürebileceğini göstermektedir.

Ayrıca, metal oksit oluşumunun yanma odası stabilitesi üzerindeki etkileri ele alınmış ve yüksek sıcaklık operasyonlarıyla ilgili riskleri azaltmak için termal yönetim ve yakıt yapısının düzenlenmesi gibi çözümler sunulmuştur. Bu araştırmanın sonuçları, ISRU alanına önemli katkılar sağlamakta ve NASA'nın Artemis programı ve diğer uluslararası ay keşif girişimleri bağlamında gelecekteki Ay görevleri için büyük önem taşımaktadır. Bu çalışma, metal bazlı hibrit roketlerin uzun vadeli Ay keşfi ve kolonizasyonu için uygulanabilir bir çözüm olarak konumlandırılmasını sağlayan ölçeklenebilir ve sürdürülebilir bir itki sistemi sunmaktadır.

ACKNOWLEDGMENTS

Firstly, I would like to express my heartfelt gratitude to my esteemed supervisor, Assoc. Prof. Arif Karabeyoğlu, who has always stood by my side during this thesis study. More than a mentor, he has supported me like a friend, and I deeply respect and thank him for this invaluable guidance.

I would also like to extend my sincere thanks to my thesis jury members, Prof. Dr. Metin Muradoğlu, Prof. Dr. Onur Tunçer, Prof. Dr. İbrahim Özkol, and Assoc. Prof. Zeynep Parlar. Their constructive suggestions, profound expertise, and constant support during the preparation of this thesis have significantly enriched its quality and value.

Additionally, I am grateful to Ali Yalçıntaş, Miray Karpat, Dr. Mehmet Kahraman and Dr. Ozan Kara, who were always there during the experimental testing phase of my thesis. Their assistance during the manufacturing and testing processes has been invaluable.

I am also deeply thankful to Müslüm Çakır, Ersin Solmaz, Erkan Solmaz, Cengiz Uygun, Erol Özdemir, Tuncay Duman, Yasir Barış Çelebi, Hasan Sönmez, and Tarık Tiryaki for their meticulous craftsmanship during the motor production phase. Their dedication to carefully manufacturing every motor component was crucial to the success of this project.

Above all, I owe immense gratitude to my beloved wife, Dr. Handenaz Dere Yelken, who motivated me during my most challenging moments and stood by me through thick and thin. Similarly, I am eternally grateful to my brother Murat Yelken, my mother Nimet Yelken, and my father İsmail Yelken. Their unwavering support, love, and encouragement as my family have been my greatest source of strength throughout this journey. I would also like to thank my close friends Duygu

Kıymaz, Umutcan Turhan, Emre Taşkın and Sarya Toprak, who were wonderful people and who showed their friendship to me during the writing phase of my thesis and during my presentation.

TABLE OF CONTENTS

LIST OF TABLES

LIST OF FIGURES

ABBREVIATIONS

CEA	Chemical Equilibrium Analysis
DAQ	Data Acquisition System
LMT	Lunar Motor Test
LOX	Liquid Oxygen
NPT	National Standard Pipe Thread
A_e	Nozzle exit area
A_{inj}	Injector hole area
A_o	Orifice throat area
A_{port}	Fuel port area
A_t	Nozzle throat area
C_d	Discharge coefficient
C_l	Specific heat capacity of the liquid ($kJ/kg \cdot K$)
C_s	Specific heat capacity of the solid ($kJ/kg \cdot K$)
c^*_{exp}	Experimental Characteristic Velocity
c^*_{theo}	Theoretical Characteristic Velocity
d_f, d_i	Final and initial port diameter
d_{th}	Nozzle throat diameter
δ_l	Thermal thickness (m)
ΔT_2	Temperature difference between melting and ambient temperature (K)
ΔT_l	Temperature difference between vaporization and melting (K)
f_{Mg}, f_{Al}, $f_{\mathrm{Na_2SiO_3}}$	Normalized volume fractions of magnesium, aluminum, and sodium silicate

I_{sp}	Specific Impulse
k_l	Thermal diffusivity of the liquid phase (m^2/s)
L	Fuel Grain Length
L_m	Latent heat of melting (kJ/kg)
MW	Molecular Weight
P_a	Atmospheric pressure
P_c	Combustion chamber pressure
P_e	Pressure at the nozzle exit
R	Gas constant
R_u	Universal gas constant
r_f	Final fuel port diameter
r_i	Initial fuel port diameter
ρ	Density
ρ_f	Fluid density
ρ_l	Density of the liquid phase (kg/m^3)
ρ_s	Density of the solid phase (kg/m^3)
T	Temperature
T_a	Ambient temperature (K)
T_c	Combustion chamber temperature
T_m	Melting temperature (K)
T_v	Vaporization temperature (K)
T_∞	Ambient temperature
η	Mass ratio used in Lunar Vehicle Optimization
η_{comb}	Combustion efficiency
η_{nozzle}	Nozzle efficiency
γ	Ratio of specific heat
$\dot{G}_{ox}$	Oxidizer Mass Flux

$\dot{m}_{ox}$	Oxidizer mass fuel rate
$\dot{m}_t$	Total mass fuel rate
$\dot{r}$	Regression rate (m/s)
$V_{\mathrm{Mg}}, V_{\mathrm{Al}}, V_{\mathrm{Na_2SiO_3}}$	Volumes of magnesium, aluminum, and sodium silicate

Chapter 1

INTRODUCTION

Lunar research has attracted the attention of humanity for a long time. The first manned mission took place in 1969 with NASA's Apollo mission, and for the first time, samples collected from the Moon by astronauts began to be brought to Earth. The Apollo 12 [NASA, 2024] mission was a pioneer in creating detailed maps of the Moon and collecting scientific data. Subsequently, the Indian Space Research Organization (ISRO) conducted research to determine the mineral components of the Moon and to discover water on the Moon's surface. Likewise, the China National Space Administration (CNSA) [CNSA, 2015] successfully implemented the soft landing technology on the Moon in 2013. It tested the ability to communicate between the rover and the orbiter on the surface of the Moon. In recent developments, the NASA Artemis program has rolled up its sleeves to conduct much more comprehensive research and even to create the scientific infrastructure for the continuation of human existence on the Moon in the long term and to establish a campus on the Moon's surface and has formed an organization with many companies among its participants. So much so that the Artemis program triggered interest in lunar research, and many multinational projects such as Lunar Gateway, LADEE (Lunar Atmosphere and Dust Environment Explorer), and Yutu-2 (Chang'e-4 Mission) were quickly put into operation.

As a part of the results of all these investigations, the locations of water ice on the Moon and the structure of the Moon's soil were examined [Zong et al., 2022, Slyuta, 2014, Hui et al., 2013, Papike et al., 1982]. The presence of water ice on the Moon is indicated by the blue-highlighted regions in Fig. 1.1, which represent areas where ultraviolet waves suggest the existence of water ice deposits.

These areas are primarily located in permanently shadowed regions near the lunar south pole, where temperatures remain low enough to preserve ice. The temperature scale on the left shows that these regions have a maximum temperature below 100 K, supporting the stability of water ice. Additionally, the off/on albedo ratio highlights areas with high reflectance variations, further confirming potential water ice deposits [Hayne et al., 2015].

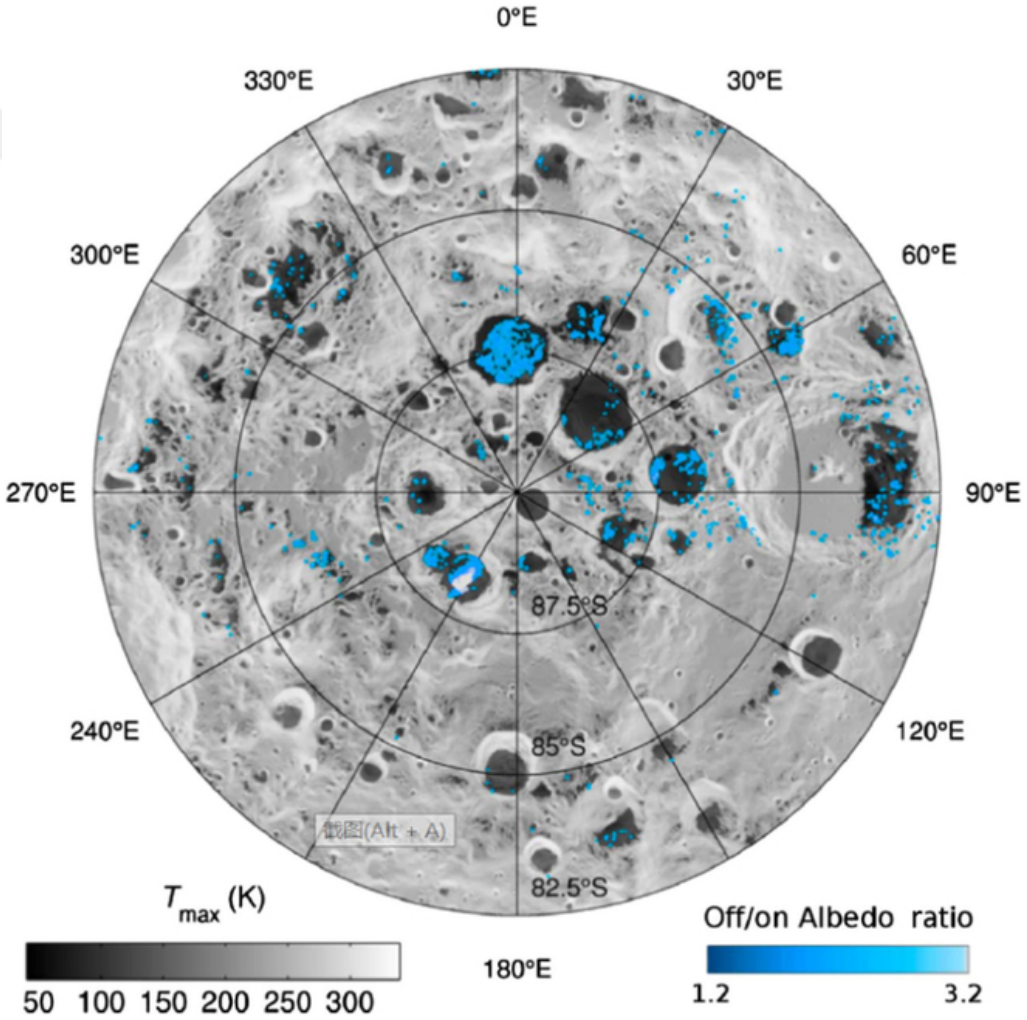

Figure 1.1: Locations where ultraviolet waves close to water ice are obtained [Hayne et al., 2015]

Although water ice is a good option for a sustainable life on the Moon, it is very costly and difficult to remove this water ice. Large tools or other methods may be required to remove this water ice [Ma et al., 2023]. Under normal conditions, it is

planned to extract this water ice and transport it to the sun-exposed side through pipelines, melt it, and then separate it into hydrogen and oxygen using electricity generated by solar panels. These components will then be utilized as fuel and oxidizer for a hydrogen-fueled rocket engine on the lunar surface. However, there are many difficulties in this plan. Chief among these difficulties is the difficulty of transporting the heavy equipment required to extract water ice from underground to the Moon. For this reason, even if such heavy equipment are transported and even if this water is somehow separated into oxygen and hydrogen, storage difficulties arise. To create all these processes, within the scope of the Artemis project, many companies such as NASA, LPI, Lockheed Martin, Paragon, Honeybee, Deep Space Industries, CSDC, NRL, OffWorld made large investments [Kornuta et al., 2019]. So much so that studies have been carried out on technologies such as thermal mining to extract this water ice. In these studies, research on technologies such as creating thermal energy by concentrating sunlight and turning water ice into liquid hydrogen and oxygen was carried out by the Colorado School of Mines (CSM) [Sowers and Dreyer, 2019].

Although the water ice found on the Moon has the potential to be the fuel of propulsion technology both between lunar orbits, to and from earth orbits, and even to Mars, when we look at the fuels currently used by major space companies such as kerosene, hydrazine, nitrogen tetroxide, xenon methane, natural gas, and hydrogen However, most of these fuels are fuels that cannot be obtained from elements found on the Moon. In addition, when we consider the daily temperature difference on the lunar surface [Jaeger, 1953], we can say that the storage problem is critical in terms of the fuel to be used. On the other hand, different solutions can be offered for both energy storage and the creation of a propulsion system. Nuclear technology or electric propulsion could be one of them. However, there is also a more viable solution. When looking at the composition of the lunar soil, Al and Magnesium are quite viable elements.

Considering the metal oxide components, it is known that Al and Mg are currently used as additives in rocket engines [Carmicino and Sorge, 2015, Karabeyoğlu,

2017, Akhter and Hassan, 2020]. In hybrid rocket engines, the features of these metal components, such as increasing the regression rate in the combustion chamber, have become an interesting field of study for hybrid rocket engines. These metal components provide advantages over hybrid rocket engines, but hybrid rocket engines generally use paraffin as the fuel component. One of the main aims of this study is to create a rocket engine using only these metal components without using paraffin. Under normal circumstances, a rocket engine composed entirely of metal components presents many problems. Problems such as combustion stability, harsh conditions in the combustion chamber, and low-performance values are the biggest obstacles to the creation of such a rocket engine fuel consisting only of metal components. Studies on designing a rocket engine fuel with only metal components on the Moon have previously been carried out by NASA [Hepp et al., 1994]. Germany has also worked on designing a rocket engine with high metal components in this field [Lips, 1976]. However, there has been no completed study on the design of a rocket engine with high performance and its use in lunar missions. Both the material technology of the period and the needs of the period requiring different orientations may have delayed the emergence of this technology. However, it seems that a real alternative to the energy and propulsion technology requirement in the NASA Artemis project may be through building a metal-based rocket engine.

The advantages that can be gained and the disadvantages that may arise from the development of a metal-fueled rocket engine, as determined through research, are summarized in Table 1. It appears that, although the use of metals as rocket fuel seems reasonable for lunar missions and the possibility of sustaining life on the Moon—due to their ease of storage, potential production from lunar regolith, and lower oxygen demand resulting from a low OF ratio—the challenges associated with this approach cannot be overlooked. The extremely high temperatures observed in the combustion chamber, the complex manufacturing process of metal components, and the high erosion levels that may occur in the nozzle and combustion chamber structures contribute to significant technical difficulties.

In this thesis, a hybrid rocket engine fueled by lunar-derived Mg and Al powders

Advantages	Drawbacks
• Widespread presence of metal compounds on the Moon • Due to the high density of metals and easy storability, it offers easy use. • While carbon-based fuels reach their most efficient state at high OF Ratios, metal-fueled hybrid rocket engines can reach their most efficient state at OF Ratio values such as 0.2. In this way, the operation of the lunar rocket engine can be ensured by using less oxygen, which is critical in the lunar mission.	• Metals cause high erosion in the combustion chamber and nozzle during combustion. • Due to the high thermal conductivity, the fuel cannot stay in solid form and liquefies, affecting the combustion dynamics. • Structurally, extra design requirements may arise due to the combustion chamber reaching high temperatures. • Metal powders can be difficult to obtain due to the presence of metals in oxide form in lunar soil. Some additional chemical processing may be required.

Table 1.1: Advantages and drawbacks of using metals as rocket fuel

was designed and tested. Different fuel compositions were evaluated using NASA Chemical Equilibrium Applications [Bonnie J and Sanford, 1996], and experimental tests were conducted to assess combustion stability, regression rates, and performance under varying O/F ratios. Additionally, an innovative igniter system was designed to facilitate ignition under lunar conditions. The results of these experiments, combined with calculations related to the use of this engine for lunar missions, provide a comprehensive foundation for metal-based propulsion technology.

Chapter 2

LUNAR RESEARCH AND PROPULSION SYSTEM EVALUATION

2.1 Lunar Investigations

Rocket engine developments are crucial for lunar missions due to the unique challenges posed by the Moon's lack of atmosphere and low gravity. These conditions necessitate specific propulsion technologies for landing, liftoff, and maneuvering on the lunar surface. In addition, variable-thrust liquid rocket engines (LREs) are essential for precise landing and take-off on the Moon. These engines allow for controlled combustion, which adjusts the spacecraft's descent speed to ensure a soft landing and safe ascent. The successful implementation of such engines was evident in historical missions like Apollo and more recent missions by other countries such as China's Chang'e 3 [Yao et al., 2023]. Many rocket engine technologies developed for use on the lunar surface are currently being implemented. In this context, some rocket engines under development are presented in Table 2.1.

Engine Name	**Fuel**	**Oxidizer**	**Company**	**Primary Use**	**Stage**	**Isp (s)**
BE-7	H_2	O_2	Blue Origin	Lunar Lander	Testing	450
RS-25	H_2	O_2	Aerojet Rocketdyne	Heavy Lift Launch Vehicle	Operational	452
Variable thrust LRE	Hydrazine	Nitrogen Tetroxide	Global	Lunar Soft Landing	Operational	290
Next Propulsion System	Xenon	None	Aerojet	Deep Space Missions	Advanced Testing	1500

Table 2.1: Rockets engines to use in moon missions, including specific impulse values.[AFR, 2023, NAS, 2023, Yao et al., 2023, Eme, 2006]

2.1.1 Cryogenic Rocket Engines on the Moon

Cryogenic rocket engines, which utilize supercooled propellants such as liquid hydrogen and liquid oxygen, offer several benefits but face with unique challenges, particularly for lunar missions.

Benefits of Cryogenic Rocket Engines on the Moon

Higher Performance: Cryogenic engines provide a higher specific impulse than other rocket engines. This means that they can achieve greater thrust per unit mass of propellant, which is crucial for the heavy lifting required in space missions [Brown, 2005].

In-Situ Resource Utilization (ISRU): The Moon has water ice, which can potentially be mined and converted to hydrogen and oxygen, the primary propellants for cryogenic engines. This could drastically reduce the need to transport propellants from the Earth, making long-term lunar missions more feasible [NASA, 2024].

Challenges

Extreme Temperatures: The Moon's surface experiences extreme temperature variations, which can be detrimental to the storage and handling of cryogenic propellants. These propellants need to be kept at very low temperatures, making their thermal management a significant engineering challenge.

Propellant Boil-off: The storage of cryogenic propellants in space environments leads to boil-off, where the stored liquid begins to vaporize. This not only results in the loss of valuable propellants but also poses risks due to increased pressure in storage tanks [Brown, 2005].

Complexity and Reliability: Cryogenic engines are mechanically complex and require high reliability, especially for missions beyond low Earth orbit. The engines must operate flawlessly after extended periods of inactivity in the harsh lunar environment [Brown, 2005].

Transport and Infrastructure: Establishing the necessary infrastructure to sup-

port cryogenic operations on the Moon includes creating robust landing pads, storage facilities, and maintenance setups, all of which must be transported or constructed on the Moon. This adds layers of complexity and cost to lunar missions.

While the use of cryogenic rocket engines on the Moon presents an opportunity to leverage higher performance and potentially local resources, it also requires overcoming substantial technological and logistical hurdles. Addressing these challenges involves not only advancements in rocket technology but also in the infrastructure and operational procedures needed for sustained lunar exploration.

2.1.2 Water-Ice Resources

Many studies are carried out on the detection of water resources on the lunar surface, and the characteristics and quantity of these water resources are investigated using different techniques [Spudis et al., 2013, Li et al., 2018]. Although these investigations are promising, the real problem begins when we want to extract these water resources and use them for energy generation. The extraction and processing of lunar water ice to produce rocket fuel (hydrogen and oxygen) are a cornerstone for sustainable space exploration, particularly for missions beyond the Moon. The process involves several stages, from ice extraction and transport to electrolysis and storage.

One promising technique for extracting water ice involves using mirrors to focus sunlight onto permanently shadowed regions of lunar craters, warming the soil and sublimating the ice into vapor. This vapor is then captured and recondensed in ice, which can be further purified and processed [Patelarchive, 2020]. Another approach utilizes a rocket mining system developed by companies such as Masten, which employs rocket engines to heat and collect ice from lunar soil. This system is designed to operate autonomously, potentially increasing the efficiency of resource collection [MastenAero, 2021].

The extreme conditions on the Moon pose significant challenges for ice extraction and fuel production. Temperature in the permanently shadowed areas can be extremely low, complicating the handling of volatile materials like hydrogen and oxy-

gen. The systems must also be robust enough to withstand the lunar environment while maintaining high levels of efficiency to justify the high cost of lunar operations. Once extracted, the ice is transported to a processing facility, where it undergoes electrolysis, splitting water into hydrogen and oxygen. These elements are then liquefied and stored as rocket propellant. Innovations in electrolysis technology on the Moon focus on minimizing energy consumption and maximizing output, as energy is a precious commodity in space.

On the other hand, the logistical framework for lunar mining operations includes the development of infrastructure such as landing pads, habitats, and storage facilities, all of which must be pre-positioned or constructed on the Moon. The costs of transporting and maintaining this equipment are substantial but mitigated over time as more infrastructure is built directly from lunar materials. The successful implementation of these technologies could revolutionize space travel, reducing the dependence on the Earth for supplies and enabling more frequent and prolonged missions. It could also pave the way for interplanetary travel, with the Moon serving as a refueling station for missions to Mars and beyond. The extraction and use of lunar water ice as rocket propellant involves complex and innovative technologies tailored to the harsh lunar environment. While challenging, these efforts are crucial for the future of human space exploration and establishing a sustainable presence on the Moon.

2.1.3 Lunar Soil

Exploring the composition of lunar soil offers a window into the moon's geological history and the potential for future lunar explorations. With recent advancements in analytical technologies, our understanding of the moon's surface material, commonly known as regolith, has deepened significantly. This fine-grained soil is not only a record of the moon's past but also a key to unlocking sustainable human presence there.

Lunar regolith consists mainly of fine dust and rocky debris formed over billions of years due to meteorite impacts. This relentless bombardment has resulted in a soil

composition that is both complex and diverse. At its core, regolith is predominantly composed of silicon dioxide, which is found in minerals such as plagioclase, pyroxene, and olivine. As shown in Table 2.2, the composition of lunar regolith varies significantly between different regions of the Moon. While maria (basaltic plains) are richer in iron and magnesium, the highlands contain higher concentrations of aluminum and calcium.

Element	**Concentration (%)**	**Found in**
Silicon Dioxide (SiO_2)	20-45	All regions
Aluminum Oxide (Al_2O_3)	3-15	Highlands
Calcium Oxide (CaO)	10-16	Highlands
Iron Oxide (FeO)	5-18	Maria
Magnesium Oxide (MgO)	3-13	Maria
Titanium Oxide (TiO_2)	0.5-10	Maria
Thorium (Th)	Trace amounts	Varied, via spectroscopy
Potassium (K)	Trace amounts	Varied, via spectroscopy
Uranium (U)	Trace amounts	Varied, via spectroscopy

Table 2.2: Typical composition of Lunar regolith based on updated studies, including data from the Chang'e-5 mission [Heiken et al., 1991, Papike et al., 1998, Che et al., 2021, Li et al., 2022].

Particularly intriguing is the volatile content in the lunar soil, especially water ice in the shadowed regions near the lunar poles. This discovery is crucial for the potential extraction of water to support life and for its use in producing rocket fuel (hydrogen and oxygen) through electrolysis. Studies like those analyzing the isotopic composition of nitrogen in lunar regolith reveal that these volatiles might have extra lunar origins, possibly delivered by comets or solar winds [He et al., 2024].
Also trace elements such as thorium, potassium, and uranium found in the regolith offer insights into the moon's thermal evolution and geological differentiation. Their presence is key to understanding internal activity and radiogenic heat production,

which are central to theories about the moon's formation and geological history [Li et al., 2022].

Detailed knowledge of lunar soil composition has significant practical applications for future missions. It serves as a foundation for plans aimed at utilizing local resources through in-situ resource utilization (ISRU), which is crucial for minimizing dependence on Earth-based material transport and ensuring the feasibility of long-term lunar missions.

2.1.4 Evaluation of Rocket Engine Technologies and Current Plans

Considering the gravitational force and geological conditions of the Moon, it currently seems to be possible to use the predominantly H_2/O_2 rocket engine. However, the mining operation brings with it many problems. Afterward, storing cryogenic fuel and oxygen may be quite problematic due to daily temperature differences on the Moon. A solution to this could be to place these tanks 1 meter underground. However, alternative methods may still need to be tried to establish a sustainable series of operations on the lunar surface. In addition, if a sustainable human presence is to be established on the lunar surface, oxygen will be essential for life support. Therefore, it will be necessary to increase the resources capable of providing oxygen.

H_2/O_2 Rocket Engine

Although it has high ISP values, using the H_2/O_2 rocket engine in lunar missions may cause some problems. Since hydrogen has particularly low density, even if it is stored under cryogenic conditions, it will require a lot of equipment support and take up volume, even though composite tank technology is advanced [Boretti, 2023]. In addition, transporting these equipment and tanks to the lunar surface will create a significant cost. These processes may cause the amount of hydrogen that can be stored to be limited, and as a result, sustainability may become problematic. Because oxygen has a higher density than hydrogen, it offers some advantages in terms of storage. However, under cryogenic conditions, the need for increased safety precautions and additional equipment imposes a significant burden.

Electric Propulsion

Electric propulsion, while highly efficient for certain types of space missions, faces with significant limitations when it comes to transporting large payloads from the lunar surface to lunar orbits. Electric propulsion systems, such as ion thrusters, generate very high specific impulse, which means they are extremely fuel-efficient over long durations. However, they produce very low thrust compared to chemical propulsion systems. This low thrust output makes it difficult to lift heavy payloads off the Moon's surface, where a significant initial thrust is required to overcome the gravitational pull. Although electric propulsion offers many advantages for long-duration, deep-space missions due to its high efficiency and lower fuel requirements, it currently lacks the thrust capability and scalable power generation needed for tasks like transporting large payloads from the Moon to orbit. This makes it less suitable for direct lunar lift-off missions compared to more traditional chemical rockets, which can generate the necessary high thrust levels instantaneously.

Metal Based Hybrid Rocket Engines

There are especially high concentrations of energetic metal components in the lunar soil, which are presented in Table 2.3. When considering the use of these energetic metals as a rocket engine, some conveniences and difficulties also arise. First of all, these compounds, which are found in metal oxide form in the lunar soil, need to be separated into metal and oxide components. There are some methods for this. In the field of materials science, the separation of compounds into their base components—particularly the separation of oxides into their constituent metal and oxygen—is a significant process. This is especially relevant for oxides such as magnesium oxide (MgO) and aluminium oxide Al_2O_3, which are pivotal in various industrial applications, from refractories to ceramics and catalysts. This thesis explores the main methods employed in the decomposition and separation of these compounds.

Electrolysis is a primary method used for breaking down metal oxides into their elemental parts. This process involves passing an electric current through the oxide,

typically when it is in a molten state, causing the oxide to decompose into its metal and oxygen gas.

Metal Oxide	**Heat of Formation(kJ/mol)**	**Molar Mass(g/mol)**
Silicon Dioxide (SiO_2)	-911.00	60.08
Aluminum Oxide (Al_2O_3)	-1675.70	101.96
Calcium Oxide (CaO)	-635.10	56.08
Iron(II) Oxide (FeO)	-272.00	71.85
Magnesium Oxide (MgO)	-601.60	40.30
Titanium Dioxide (TiO_2)	-944.70	79.87

Table 2.3: Heat of formation and molar masses of metal oxide components found in lunar regolith [Chase, 1998, Bartel and Coble, 1991, Kubaschewski et al., 1993].

For magnesium oxide, at the temperature of 2400°C, molten MgO can be electrolyzed to produce metal magnesium and oxygen. This high-temperature process requires specialized equipment to handle the extreme conditions [Mohandas, 2013]. For Aluminum the Hall-Héroult process is a well-known application of electrolysis where aluminum oxide is dissolved in molten cryolite and decomposed to form metal aluminum at the cathode and oxygen at the anode.

The other method is carbothermic reduction. Carbothermic reduction involves reducing metal oxides using carbon or carbon monoxide as a reducing agent. This method is particularly effective at high temperatures where the carbon reacts with the oxygen in the oxide to form CO or CO2, leaving behind the metal. Reduction of MgO using carbon at temperatures around 2000°C can yield magnesium vapor and carbon dioxide. The magnesium vapor can then be condensed into solid metallic magnesium. Although more challenging due to the strong bond between aluminum and oxygen, researchers have been exploring variations of carbothermic processes that might make this method viable for aluminum production in the future [Schilm et al., 2021].

Also, chemical reduction is an option. Chemical reduction methods involve using more reactive metals as reducing agents to displace less reactive metals from their oxide forms. Magnesium oxide can be reduced using silicon at high temperatures, producing magnesium vapor and silicon dioxide. More reactive metals, such as sodium, can be used to reduce aluminum oxide to aluminum at temperatures above 800°C, although this is less common due to the expense and reactivity of sodium.
Due to the Moon's lack of atmosphere and daily temperature differences, one of the possible possibilities is thermal decomposition. This method can decompose some metal oxides directly by heating (calcination). However, this method is generally limited to oxides that decompose at temperatures lower than their melting points. These oxides are very stable and do not easily decompose into metal and oxygen through heating alone, making thermal decomposition impractical for these compounds. However, there is still a high probability that these components will be separated by thermal decomposition on the Moon's surface.
Assuming that the metal components can be separated and oxygen can be easily stored, problems arise regarding the operability and harsh operating conditions of a rocket engine. First of all, the metal components that burn in the combustion chamber must leave the combustion chamber in the gas phase. Otherwise, the combustion chamber will not be pressurized or the engine performance will be low due to unburned components leaving the combustion chamber in the liquid phase. When the appropriate combustion chamber conditions are met, the combustion chamber may suffer sudden structural damage due to the extremely high temperature values reached in the combustion chamber, which will require passive or active cooling of the combustion chamber.

Comparison of Storage of the Fuels and Oxidizers

Efficient storage of fuels and oxidizers is a critical factor in the design and operational feasibility of rocket propulsion systems. While both hydrogen-oxygen and metal-based propellant systems rely on oxygen as an oxidizer, they differ significantly in terms of storage requirements and handling complexity.

As shown in Table 2.4, metals such as magnesium and aluminum offer significant advantages in terms of storage because they exist in solid form under standard conditions. Unlike hydrogen, which requires cryogenic storage at extremely low temperatures, magnesium and aluminum can be stored at ambient conditions without the need for specialized tanks or insulation. This eliminates the challenges associated with hydrogen boil-off, which leads to fuel loss over time due to evaporation, making long-term storage and transportation more complex.

Additionally, the density of hydrogen (0.071 g/cm^3) is significantly lower than that of metallic fuels, meaning that a much larger volume of hydrogen is required to store an equivalent amount of energy. This necessitates high-pressure tanks or cryogenic storage systems, increasing the overall weight and complexity of the propulsion system. Oxygen, on the other hand, although required in both systems, still necessitates cryogenic storage, which poses additional logistical challenges.

By utilizing metallic fuels, it is possible to develop more compact, energy-dense propulsion systems that reduce tank weight, thermal insulation requirements, and storage constraints. This, in turn, contributes to lighter spacecraft designs and enhanced mission feasibility, particularly for long-duration space exploration missions where fuel storage efficiency is a major concern.

Substance	**Density (g/cm^3)**	**Tank Requirement**	**Cryogenic Conditions**
Magnesium	1.74	No	No
Aluminum	2.70	No	No
Oxygen	1.14	Yes	Yes
Hydrogen	0.071	Yes	Yes

Table 2.4: Density and storage requirements for selected elements and compounds

2.1.5 Hybrid Rocket Engine Fundamentals

Hybrid rocket technology, recognized for its inherent safety, reliability, and eco-friendly attributes, stands as an intriguing field within aerospace propulsion. These

systems distinctly store propellants in different physical states — typically, with the oxidizer in liquid or gaseous form, and the fuel as a solid. This segregation is beneficial for several reasons.

The oxidizer, often housed in an aluminum or stainless steel tank, flows into the combustion chamber through meticulously designed systems, with well controlled the pressure and flow rate to ensure proper mixing and combustion. The choice of materials for the components, such as brass for injectors due to its high-temperature resilience, reflects the thoughtful engineering that addresses the thermal and mechanical challenges these rockets face.

Moreover, hybrid rockets utilize composite materials for their pressurization systems, often employing helium as the pressurizing agent, demonstrating the industry's shift towards materials that offer high strength-to-weight ratios while also being functional in extreme conditions.

The combustion process in hybrid rockets is a focal point — the design of the fuel grain, for example, with circular port configurations, plays a crucial role in ensuring efficient and high regression rates. The materials used for nozzles, such as graphite, are selected for their ability to withstand high thermal loads.

From a historical perspective, the development of hybrid rocket technology has seen various iterations and milestones. Early efforts by pioneers like Sergei Korolev and Mikhail Tikhonravov, as well as subsequent advancements through the mid-20th century, laid the foundational work for the rockets we see today [Sutton and Biblarz, 2017]. These developments have been marked by both triumphant achievements and setbacks that subsequently have driven innovation and learning.

The contemporary landscape of hybrid rocket propulsion sees a variety of commercial entities entering the fray, each contributing to the evolving narrative of space exploration with their unique designs and technological advances. These modern endeavors strive to realize the potential of hybrid systems for cost-effective and accessible space travel.

The advantage of the hybrid rocket engine is that it keeps the fuel in solid form and does not require any extra tanks for fuel. The fuel in the combustion chamber

starts to burn at a certain regression rate [Sutton and Biblarz, 2016]. Besides paraffin Wax being the most widely used hybrid rocket engine, components such as HTPE (Hydroxyl-terminated polyether), Plexiglass (Lucite), PB (polybutadiene) can also be used as fuel. In addition, nitrous oxide is chosen as the oxidizer because it is in liquid form at room conditions.

The representation of the entrainment process in hybrid rocket motors is presented

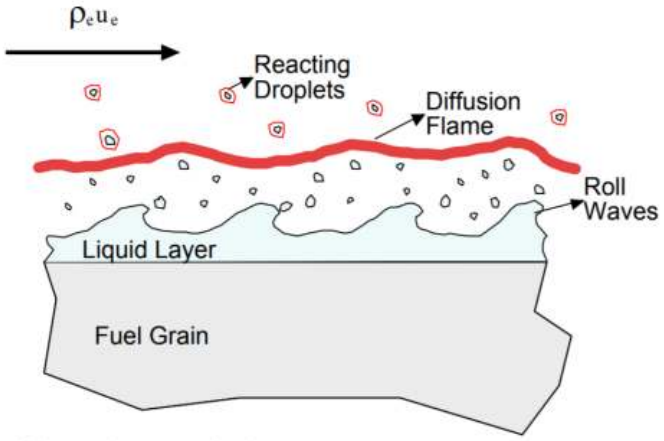

Figure 2.1: Entrainment mechanism of hybrid rocket engines [Karabeyoglu et al., 2005a]

in Fig. 2.1. In this figure, the fuel grain undergoes heating and forms a liquid layer on its surface due to the interaction with the oxidizer flow. As the liquid layer evaporates, reacting droplets are entrained into the flow and contribute to combustion. Above the surface, a diffusion flame forms where fuel vapor mixes with the oxidizer, leading to sustained burning. Additionally, roll waves appear on the surface, enhancing mass transfer and affecting the overall combustion efficiency. When comparing paraffin wax to traditional polymeric fuels, the entrainment process allows paraffin to achieve a regression rate three to five times higher at the same oxidizer mass flux. This is attributed to the high specific burning area provided by the droplets formed from the melted wax. Additionally, paraffin-based fuels begin to melt and pyrolyze at temperatures above 40 °C, aiding the generation of droplets that evaporate and burn, thereby fostering the combustion process. Due to these

properties, paraffin-based fuels experience less convective heat transfer impedance, resulting in a lower blocking effect than those seen with non-liquefying fuels.
Different methods are applied to increase the low regression rate in the hybrid rocket engine. The most important of these methods is the addition of nano or micro-sized metals to the fuel. It is aimed to increase the regression rate by adding metals such as aluminum, magnesium, or iron [Yamazaki et al., 2022, Risha et al., 2002, Arifah Binti Mohamad Jamil et al., 2023, Karabeyoglu and Arkun, 2014].

Chapter 3

LUNAR PROPELLANT DESIGN AND THERMOCHEMICAL ANALYSIS

3.0.1 Component Selection

This chapter aims to present a sustainable hybrid rocket engine that can be supplied in-situ by lunar resources. For this reason, emphasis was placed on aluminum and magnesium, which are abundant in the lunar soil and have high energetic values. Magnesium and aluminum are both highly reactive metals that are capable of undergoing vigorous exothermic reactions with oxygen, releasing a significant amount of energy in the process. These reactions are characterized by several steps, known as reduction stages, which play a key role in the combustion process used in rocketry. Magnesium burns in oxygen with a bright white flame and, at sufficient temperatures, can even burn in carbon dioxide. The reaction is quite straightforward, with magnesium combining with oxygen to form magnesium oxide (MgO). The reaction is provided in Eq. 3.1.

$$2\mathrm{Mg} + \mathrm{O_2} \rightarrow 2\mathrm{MgO} \tag{3.1}$$

This reaction releases around 24.7 kJ/g of energy, which explains why magnesium is used in applications requiring intense heat and light.

Aluminum also reacts with oxygen to form aluminium oxide (Al2O3), often called alumina. The reaction is highly exothermic and releases about 31.0 kJ/g of energy. The overall reaction is provided in Eq. 3.2:

$$4\mathrm{Al} + 3\mathrm{O_2} \rightarrow 2\mathrm{Al_2O_3} \tag{3.2}$$

Due to the high energy release, aluminium is used as a fuel in solid rocket propellants.

Both aluminium and magnesium, when ignited, undergo a series of complex reactions involving oxidation and subsequent reduction processes. Initially, the metal reacts with oxygen to form a stable metal oxide layer. Under elevated temperatures, this oxide can further interact with excess metal, leading to the formation of suboxides in intermediate reduction stages. For instance, in the case of magnesium, MgO may react with Mg to produce sub-stoichiometric oxides, denoted as MgO_x where $0 < x < 1$. These reactions progress through multiple reduction pathways before ultimately reaching a thermodynamically stable oxide composition. For the combustion of magnesium and aluminium, especially in the context of hybrid rocket motors, the combustion mechanism is of paramount importance because it directly influences the efficiency and stability of the motor.

Magnesium combustion in an oxidizing atmosphere is a vapor-phase-controlled process. This has been supported by experimental studies showing that the ignition and combustion of metallic magnesium are influenced by particle size and that smaller particles can dramatically increase the flame spread rate. The combustion process of magnesium typically involves an initial slow oxidation phase, followed by a rapid reaction period and culminating in a smoldering phase that continues beyond the melting point of magnesium. In oxidizing atmospheres, the reaction is controlled by the diffusion rate of oxygen, whereas in pure oxygen, it is controlled by the vaporization rate of magnesium vapor. This suggests a significant difference in the combustion mechanism depending on the oxidizing environment [Yang et al., 2021, Nam et al., 2022]. Aluminium combustion, particularly in aluminium-based alloys such as Al-Mg, has been found to have good ignition response and efficient combustion characteristics, largely due to the lower ignition temperature of these alloys compared to pure aluminium powder. Alloying aluminum with metals like magnesium can improve the combustion calorific value and the flame speed, potentially leading to higher specific impulse efficiency in solid rocket propellants [Xin et al., 2023].

Also, the ignition and combustion of aluminum/magnesium alloy particles in high-pressure oxygen environments, relevant for rocket engine applications, have been

investigated to measure the ignition delay and combustion times, providing valuable data for the development of ignition models and enhancing the understanding of the combustion process at various pressures and temperatures [Roberts et al., 1993]. These extensive archives of information on magnesium and aluminum show that their use as fuel in rocket engines is quite feasible.

MgO Decomposition

Magnesium oxide (MgO), known for its high melting point and stability, can be decomposed into magnesium and oxygen through several advanced methods, each suitable for different industrial needs and outcomes.

One common method is thermal decomposition, which involves heating magnesium compounds like magnesium carbonate or hydroxide to high temperatures. This process not only yields magnesium oxide but is crucial in manufacturing refractory materials due to the compound's ability to withstand high temperatures [Hornak, 2021].

Electrolysis is another technique, particularly significant in the synthesis of high-purity magnesium. This method involves the decomposition of magnesium oxide at high temperatures in an electrolyte medium, under the influence of an electric current. This method is noted for its ability to produce magnesium metal directly from MgO.

Innovative chemical methods like sol-gel, hydrothermal, and microwave-assisted sol-gel processes are also used to produce MgO with specific physical properties, such as nanoscale particle sizes and increased surface area. These properties are particularly beneficial for applications requiring high reactivity and surface area, such as in catalysts and environmental applications [Todan et al., 2023].

Each method has its distinct advantages and limitations based on the required purity, particle size, and intended use of the magnesium oxide produced. For instance, sol-gel processes are favored for their control over particle characteristics, making them ideal for specialized applications in electronics and catalysis [Kemical-info, 2024].

Al_2O_3 Decomposition

Aluminum oxide (Al_2O_3), commonly known as alumina, is a highly stable ceramic material with exceptional mechanical strength, thermal stability, and chemical resistance, making it suitable for various high-temperature applications. It can be decomposed into its elemental components, aluminum, and oxygen, through several methods, each suited to specific industrial needs.

1. Thermal Decomposition: One of the primary methods for decomposing aluminum oxide is thermal decomposition. This process involves heating alumina to high temperatures where it dissociates into aluminum metal and oxygen gas. This method is particularly important for extracting aluminum in the metallurgy industry.

2. Electrochemical Decomposition: Electrolysis or electrochemical decomposition is another critical method, especially noted for its role in the Hall-Héroult process for aluminum production. Here, aluminum oxide dissolved in molten cryolite is decomposed using an electrical current to yield pure aluminum at the cathode and oxygen at the anode [Ludwig and Burke, 2022, Hatfield et al., 2024].

3. Carbothermic Reduction: This method involves reducing aluminum oxide with carbon at temperatures around 2000°C. The carbon acts as a reducing agent, pulling oxygen away from aluminum, which can then be collected as metallic aluminum. This method is less common than electrolysis but is used in conditions where electrical methods are less feasible.

4. Chemical Vapor Deposition (CVD): CVD is a technique used not only to create thin films of alumina but also in some cases to decompose these films back into aluminum and oxygen under specific conditions. It is primarily used for coating processes or to create high-purity alumina films for electronic applications [Ludwig and Burke, 2022].

These methods reflect the versatility and importance of aluminum oxide in industrial applications, ranging from primary metal extraction to advanced manufacturing processes [Misra, 2013]. Each method has its own advantages, tailored to specific production requirements and material properties.

3.0.2 Combustion of in-situ fuels

When considering a fuel structure composed entirely of metal fuels, several challenging combustion conditions must be carefully addressed. One of the primary challenges is ensuring that combustion products are effectively expelled from the combustion chamber through the nozzle and out of the engine in a sustainable manner. Another concern is the erosion effect that metal components can cause within the combustion chamber and nozzle, potentially leading to material degradation over time. However, one of the most crucial parameters affecting engine efficiency is whether the metal oxides formed after the combustion of magnesium and aluminum leave the combustion chamber in gaseous form. If magnesium oxide and aluminum oxide do not reach a gaseous state within the chamber, this can hinder the pressurization of the combustion chamber and significantly reduce combustion efficiency. The boiling points of the proposed fuel components and their respective metal oxide forms are presented in Table 3.1. The critical threshold that the combustion chamber must reach is determined by the boiling point of magnesium oxide, as it has the highest value. Therefore, both the combustion chamber and nozzle throat need to reach at least 3600 °C Additionally, the Isp value is a key parameter in designing the combustion chamber, as achieving high Isp and high temperatures is essential for sustainable operation. To understand the impact of metals on the combustion chamber and rocket performance, the O/F ratio vs. Isp graph is shown in Fig. 3.1.

The graph reveals several insights into the effects of adding aluminum (Al) and magnesium (Mg) to the fuel mixture, as well as the influence of varying their ratios on vacuum Isp. The evaluation of the results obtained from the analyzed mixture ratios is presented below.

High Magnesium Content (%80 Mg, %20 Al, O_2): Mixtures with a high percentage of magnesium achieve relatively high Isp values at lower O/F ratios, peaking around 350 seconds in vacuum Isp. This performance diminishes as the O/F ratio increases, indicating that magnesium-rich fuels perform best in fuel-rich conditions. Magnesium's faster burn rate at lower temperatures provides a substantial thrust boost, which is advantageous for applications requiring quick ignition and relatively

Material	**Formula**	**Vaporization Temperature (°C)**
Magnesium	Mg	1107
Aluminum	Al	2467
Magnesium Oxide	MgO	3600
Aluminum Oxide	Al_2O_3	2977

Table 3.1: Vaporization temperatures of metals and their oxides [Doe and Smith, 1975, Brown and Green, 2016b, Wikipedia Contributors, nd, Brown and Green, 2016a].

moderate temperature ranges.

Paraffin, O_2: Pure paraffin has a moderate peak Isp, reaching around 370 seconds. This mixture shows stable Isp values over a broad range of O/F ratios, which suggests that paraffin-based fuels offer greater flexibility with minimal performance variation.

Aluminum-Enhanced Mixtures (%80 Paraffin, %20 Al, O_2): Adding aluminum to paraffin increases Isp values to around 380 seconds at O/F ratios near 2. Aluminum's high combustion temperature and energy density contribute to this increase in Isp. However, as O/F ratios rise, Isp values decrease more quickly than with magnesium-based fuels. This indicates that aluminum-enriched mixtures are better suited for applications where high peak performance is desired within a limited O/F range.

High Aluminum Content (%60 Paraffin, %40 Al, O_2): Increasing the aluminum content further results in the highest Isp values observed in this chart, with peaks reaching approximately 410 seconds. This confirms aluminum's potential in significantly enhancing specific impulse, albeit with trade-offs in operational temperature and ease of ignition due to its higher combustion temperature.

In designing the engine, one critical design consideration is ensuring ease of ignition. Due to aluminum's high ignition temperature, it is generally preferable to keep the aluminum content relatively low. However, since aluminum can significantly

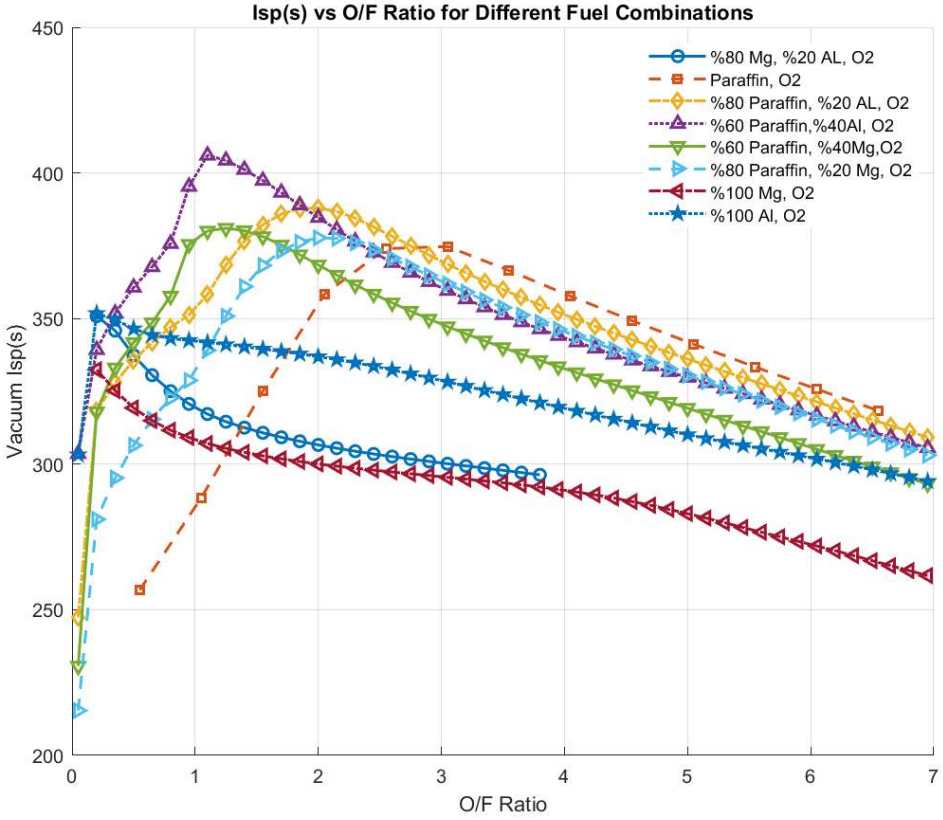

Figure 3.1: Effect of O/F ratio on vacuum Isp for different fuel combinations. The graph compares the specific impulse (Isp) in vacuum for various fuel compositions with varying magnesium (Mg) and aluminum (Al_2O_3) content in combination with oxygen (O_2) and paraffin. Area Ratio=100, $P_c = 10bar$

enhance Isp values, finding the optimal balance that enables both high Isp and efficient ignition at lower temperatures is essential. The properties of mixtures with different Mg-Al ratios are shown in Fig. 3.2. Here, values marked in red represent temperatures below the boiling point of magnesium oxide.

For engine design, it is crucial to consider the temperatures in the combustion chamber and nozzle throat. Combustion products that reach the nozzle throat and exit in gaseous form do not typically cause extensive deformation to the combustion chamber geometry. Therefore, it is acceptable for combustion products to be in liquid form at the nozzle exit, as this does not pose significant risks. However, it

Mg(%)	Al(%)	O/F Ratio	Ivac(s)	T1(K)	T2(K)	T3(K)
95	5	0.2	335.98	3749.9	3607.6	2529.6
90	10	0.2	340.87	3965.5	3801	2495.4
85	15	0.20	347.19	4057.7	3913.6	2427.6
80	20	0.20	350.76	4102.8	3949.6	2504.4
75	25	0.20	352.49	4132.2	3988.2	2575.4
70	30	0.25	353.21	4222.4	4077.3	2871.1
65	35	0.25	353.51	4240.6	4094.3	2900.6

Table 3.2: Combustion chamber, nozzle throat, and nozzle exit temperatures along vacuum Isp values for different Mg-Al fuel mixtures based on O/F ratio. T1: Combustion chamber temperature, T2: Nozzle throat temperature, T3: Nozzle exit temperature. Red-highlighted temperature values indicate conditions where combustion product temperatures fall below the vaporization temperatures of the metal oxides, whereas green-highlighted values exceed these vaporization temperatures. Data obtained using NASA CEA [Bonnie J and Sanford, 1996].

is essential to avoid clogging in the nozzle or accumulation of liquid combustion products in the combustion chamber. From Fig. 3.2, it is evident that mixtures with %85 Mg, %15 Al and %80 Mg, %20 Al compositions are suitable candidates for testing. These mixtures offer the potential to reach the necessary temperatures while achieving efficient performance and avoiding the issues associated with liquid-phase oxides in the chamber or nozzle.

3.0.3 Binder Selection

One of the targeted outputs within the scope of this study is that the elements found on the Moon play an active role in the fuel production process. Therefore, a binder that is suitable for this purpose and supports performance values must be selected. Some binders actively used in the industry are given below.

Epoxy Resins

Epoxy resins are another commonly used binder for binding metal powders. These resins consist of a mixture of epoxy resin and hardening agents. Epoxy resins provide high strength, chemical resistance, and durability. They can also be formulated to suit various application methods.

Other Polymer Binders

Polymer-based binders can also be used to hold metal powders together. These binders are typically composed of various polymers such as polyethylene, polyvinyl alcohol, or polyurethane. Polymer binders offer properties such as flexibility, adhesion, and processability.

Sodium Silicate

Sodium silicate, known for its binding properties, is extensively used across various industries, including its application as a binder for metal powders to enhance product integrity and performance. The following chemical reaction represents the formation of sodium silicate:

$$SiO_2 + 2NaOH \rightarrow Na_2SiO_3 + H_2O \tag{3.3}$$

In this reaction, sodium hydroxide (NaOH) reacts with silica (SiO_2) to form sodium silicate (Na_2SiO_3), along with water (H_2O) as a byproduct. Sodium silicate solutions typically contain water, which gives the material its liquid or gel-like form. When heat is applied to the solution, the water evaporates, initiating a solidification process. The removal of water through heating facilitates the transition of sodium silicate into a solid matrix. This solidification occurs due to the condensation of silicate anions, which forms a rigid, glass-like structure. This process is particularly advantageous in metal powder applications, where sodium silicate acts as a binder. Upon evaporation of water, the residual sodium silicate creates strong physical bonds

between metal particles, improving the mechanical strength and structural stability of the composite material.

Furthermore, the chemical composition of the resulting sodium silicate matrix plays a crucial role in the binding process. The remaining sodium silicate bonds ensure that the particles are held together firmly, offering thermal and mechanical resilience. This property is especially useful in high-temperature environments where traditional organic binders may fail. As a result, sodium silicate solutions provide both a chemically robust and physically durable binding mechanism, making them a critical component in advanced material manufacturing processes.

- Thermal Stability: Sodium silicate remains stable at high temperatures, typically up to 1100°C, which is essential for high-temperature processes such as sintering in the metal powder industry [Wang et al., 2020, Wang et al., 2019].

- Chemical Durability: Resistant to water and many chemicals, sodium silicate can protect bound materials from environmental degradation.

- Ease of Use and Cost-Effectiveness: Sodium silicate is relatively easy to handle and mix with other components, and it is more cost-effective compared to other organic binders.

Sodium silicate is used as a binder in refractories and ceramics to improve their mechanical strength and durability [Goldstein et al., 2009]. Also, sodium silicate acts as a binder in the sintering of metal powders, helping to form a rigid structure without compromising the metallic properties [Luo et al., 2023]. The fact that the water solution of sodium silicate is in liquid form and that all the elements contained in it can be obtained using lunar resources, as well as being inorganic, is sufficient for it to be used in this study. The properties of the sodium silicate solution used during the experimental studies in this thesis are presented in Table 3.3.

Using sodium silicate as a binder on the Moon's surface is a compelling idea, primarily due to its availability and practical benefits. Sodium silicate, often called

Property	**Value**
Composition	Sodium oxide (Na_2O), Silicon dioxide (SiO_2), Water (H_2O)
Appearance	Transparent to white, viscous liquid or solid
Density	Approximately 2.4 g/cm^3 (solid)
Melting Point	Approximately 1088°C (solid form)
Solubility	Soluble in water, reacts to form a gel

Table 3.3: Structural properties of sodium silicate. Data derived from various sources: composition from BYJU'S [BYJU'S, 2024], appearance and density from Science Notes [Notes, 2024], and solubility details from Science Madness [Madness, 2024].

liquid glass, consists mainly of sodium, silicon, and oxygen, elements that are abundant in lunar soil. This makes the in-situ production of sodium silicate feasible, potentially reducing the need for material transport from Earth. Sodium silicate's ability to form a gel that binds materials together when reacting with water makes it an ideal candidate for lunar construction projects. This property would be particularly valuable in the Moon's harsh environment, where temperature extremes and radiation pose challenges to structural integrity. The binder's high-temperature resistance and environmental friendliness further enhance its suitability for such extraterrestrial applications. Moreover, the simplicity of using sodium silicate, combined with its cost-effectiveness, adds to its appeal as a construction material on the Moon. Its use could support various construction activities, from building habitats to paving surfaces, providing a durable and resilient infrastructure necessary for sustaining lunar bases. Thus, exploring sodium silicate's applications on the Moon could be a significant step toward sustainable extraterrestrial development.

3.0.4 Fuel Grain Production from Metal Powders

In the production of fuel grain, 44 μm magnesium and aluminum powders were used at 75% and 20% by weight, respectively. Sodium silicate water solution was added at 5%. Classic household mixers were used as the mixing method. Although

ball milling was initially considered for the mixing process, significant issues were encountered during its application.

The primary challenge with ball milling was the behavior of the sodium silicate solution. When introduced into the ball mill, the solution adhered to the milling balls and caused aluminum and magnesium powders to clump together around the balls. This resulted in severe agglomeration, making it impossible to achieve a uniform distribution of the fuel components. Additionally, despite extensive cleaning efforts, the residual material stuck to the balls could not be fully removed, leading to contamination and inconsistency in subsequent trials.

This irregularity in the mixture not only compromised the homogeneity of the fuel grain but also posed significant difficulties in maintaining the desired stoichiometry and physical properties of the final product. Considering these limitations, the production process was carried out using a kitchen mixer instead. This method proved to be more effective in creating a uniform and consistent mixture without the issues of agglomeration and contamination observed in the ball milling process.

The fuel preparation process and metal powders properties which are used in the tests are presented in Fig. 3.2, Table 3.4 respectively.

Supplier	**Material**	**Particle Size (μm)**	**Purity (%)**
Nanokar	Aluminum	44	99.99
Nanokar	Magnesium	44	99.99

Table 3.4: Specifications of metallic powders used in propellant design

As mentioned, the mixing step was carried out with any conventional household mixer. The important thing in this process is to obtain a uniform mixture and to ensure that the sodium silicate touches the entire mixture. Mixing time is automatically maintained at around 2 hours. Mixing time was also tested as 30 minutes, 1 hour and 1.5 hours and in the case of a mixing time below 2 hours, cracks in the fuel and breakage during removal from the mold were observed in the visual inspections as presented in Fig 3.3. In this respect, it was important to keep the mixing time at

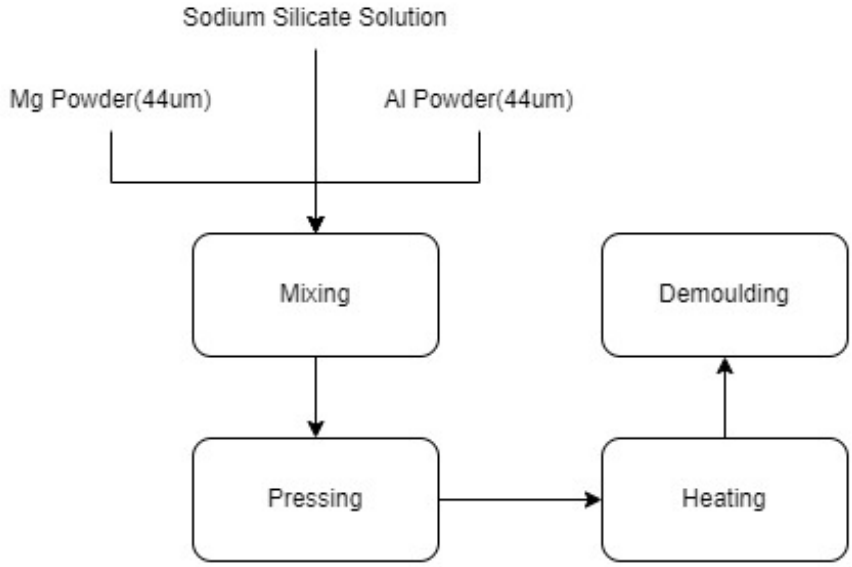

Figure 3.2: Fuel preparation steps

2 hours or more. After the mixing stage, the fuel molding stage is started using a

Figure 3.3: Sample subjected to mixing for 1 hour

mold made entirely of brass material, a visual of which is shown in Fig. 3.4, and the powder mixture is poured into this mold. This mold is then pressed with the help of a press. During the pressing stage, it is kept at 100 bar pressure for 3 hours. In this way, the air gaps in the fuel are closed. The main reason for applying pressure for 3 hours is that major changes in the press pressure begin to completely cease. The gauge pressure in the press was re-pressurized to maintain it at 100 bar continuously for the first 2 hours. However, when the 3rd hour was entered, the press pressure gauge began to decrease no longer. Therefore, a period of 3 hours was deemed appropriate for fuel production. The image of the mold mechanism used for these processes is presented in Fig. 3.4.

Figure 3.4: Brass mold

After the pressing stage, the fuel is kept in the oven at 150 °C degrees for 2 hours. Thus, the water of the sodium silicate solution in the fuel is evaporated, and a rigid structure emerges. Afterward, the fuel is removed from the mold. As mentioned

before, brass was chosen as the mold material. One of the most important reasons for choosing brass is to ensure that the fuel grain can be separated from the mold more easily. However, a press must still be used to separate the fuel from the mold. At this stage, additional mechanical parts designed to separate from the mold were used and these mechanical parts were used to separate the fuel from the brass mold using the press. After all these processes, fuel is obtained as shown in Fig 3.6. On the other hand, in the tests performed when the fuel remained in the oven for less than 2 hours, it was determined that not all the water in the sodium silicate solution evaporated, and this situation caused parts to break off from the fuel during the removal of the fuel from the mold. The image of the fuel removed from the mold after 1 hour of baking is presented in Fig. 3.5.

Figure 3.5: Fuel sample left in the oven for 1 hour

All of these steps were also carried out for fuel samples containing 10% binder. As a result of the fuel grade preparation phase, 9 samples were obtained. The obtained samples are presented in Table 3.5.

Figure 3.6: Fuel grade(composition: %75 Mg - %20 Al - %5 binder)

3.0.5 Error Analysis for Density Measurements

The density of the fuel samples (ρ) is calculated using the formula:

$$\rho = \frac{m}{V},$$

where m is the mass of the sample, and V is its volume. The relative error in density measurement (E_ρ) can be expressed as:

$$E_\rho = E_m + E_V,$$

where E_m is the relative error in mass measurement, and E_V is the relative error in volume measurement.

The mass (m) of the sample was measured using a digital scale with a precision of $\pm 0.1\,\text{g}$. For a typical sample mass of $300\,\text{g}$, the relative error in mass measurement

Sample Number	**Press Pressure(Bar)**	**Mg Ratio(%)**	**Al Ratio(%)**	**Binder Ratio(%)**	**Density (kg/m³)**
1	100	75	20	5	947 ± 28.71
2	100	75	20	5	979 ± 29.68
3	100	75	20	5	920 ± 27.89
4	100	75	20	5	949 ± 28.77
5	100	71	19	10	973 ± 29.50
6	100	71	19	10	976 ± 29.59
7	100	71	19	10	983 ± 29.81
8	150	75	20	5	1217 ± 36.91
9	150	71	19	10	1249 ± 37.88

Table 3.5: Composition of samples with density error margins.

is calculated as:

$$E_m = \frac{\Delta m}{m} \times 100 = \frac{0.1}{300} \times 100 \approx 0.033\%.$$

The volume (V) of the sample was determined based on its dimensions (diameter and height), assuming a cylindrical shape:

$$V = \pi \left(\frac{d}{2}\right)^2 h.$$

The relative error in volume measurement is given by:

$$E_V = 2 \cdot E_d + E_h,$$

where $E_d = 1\%$ and $E_h = 1\%$ are the relative errors in diameter and height measurements, respectively. Substituting these values:

$$E_V = 2 \cdot 1 + 1 = 3\%.$$

Combining these errors, the total relative error in density measurement is:

$$E_\rho = E_m + E_V = 0.033 + 3 \approx 3.033\%.$$

Thus, the density measurements are subject to a total relative error of approximately 3.03%, which accounts for uncertainties in both mass and volume measurements.

3.0.6 Fuel Grade Properties and Combustion Stability Relationship

High-density metal fuels are designed to minimize porosity, which is crucial for maintaining the structure of the fuel grain during pressurization of the combustion chamber. Metal fuels, however, present a unique challenge due to their high thermal conductivity. When ignited, the rapid heat transfer throughout the metal can lead to a sudden phase change from solid to liquid. This rapid liquefaction might result in the fuel exiting the combustion chamber too quickly, leading to unburnt fuel and a loss of combustion efficiency. On the flip side, metal fuels that are not sufficiently compacted during manufacturing may have lower density, leading to an increased risk of mechanical failure. During the intense environment of combustion, these less dense fuels are more susceptible to fracturing. Fragments from such breakdowns can obstruct the nozzle, disrupting the flow of exhaust gases, damaging the motor structure, and severely impairing the stability of combustion.

Chapter 4

DEVELOPMENT OF HYBRID ROCKET MOTOR

4.1 Fuel Grade Production

In the production of fuel grains, 44 μm magnesium and aluminum powders were used at 75% and 20% by weight, respectively, with sodium silicate water solution added at 5%. During the curing process, the water in the sodium silicate solution evaporates, leaving behind a dry composition.

After water evaporation, the final composition of the fuel grain is as follows:

- Magnesium: 76.53% by weight,
- Aluminum: 20.41% by weight,
- Sodium silicate (anhydrous): 3.06% by weight.

The sodium silicate solution contained 40% water, which vaporized during the curing process. The remaining solid phase consisted of a combination of sodium oxide (Na_2O) and silicon dioxide (SiO_2), providing a durable binder for the fuel grain structure.

The fuel production process includes the following stages:

1. Mixing Powders
2. Adding sodium silicate solution
3. Continue mixing for 2 hours
4. Pouring the powder mixture into the mold

5. Pressing fuel using a press

6. 2-hour baking process to evaporate the water in sodium silicate

7. Removing the fuel from the mold

As mentioned, the mixing step was carried out with any conventional household mixer which is presented in Fig 4.1. The important thing in this process is to obtain a uniform mixture and to ensure that the sodium silicate touches the entire mixture.

Figure 4.1: Classical type of mixer

After the pressing stage, the fuel is kept in the oven at 150 degrees for 2 hours, thus the water of the sodium silicate solution in the fuel is evaporated and a rigid structure emerges. Afterwards, the fuel is removed from the mold. After all these processes, fuel is obtained as shown in Fig 3.6.

4.1.1 Mechanical Property Testing of the Fuel Samples

The mechanical properties of the fuel and the effect of the binder on these properties were observed through some structural tests after the production of the fuel. A compression test was performed on the fuel using a hydraulic press at a compression speed of 0.1 mm/minute [De Melo et al., 2020]. Two different samples were used during these tests. 5% binder was used in one of the samples, and 10% binder was

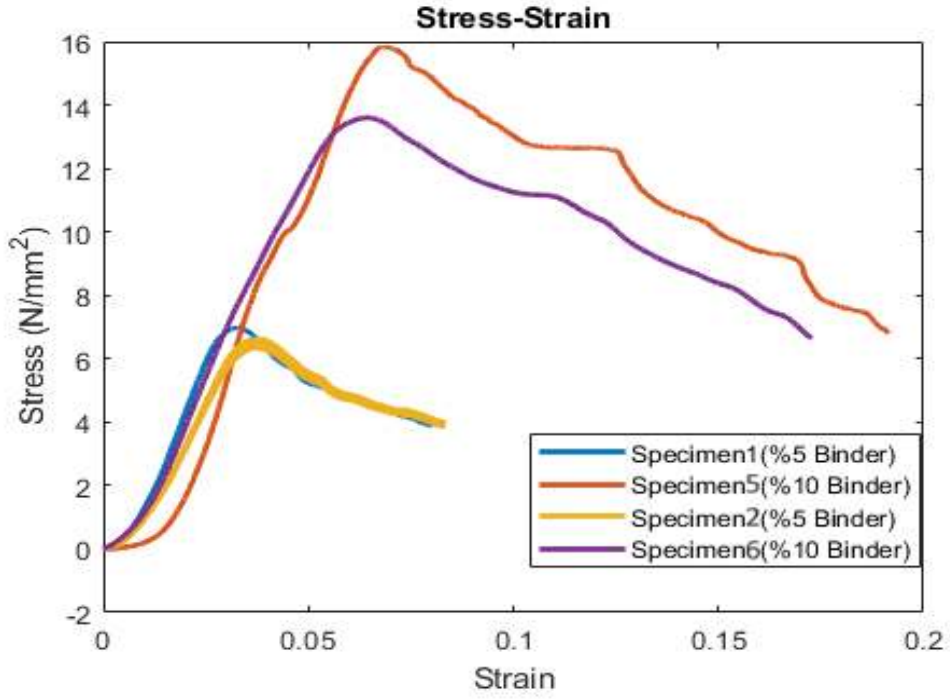

Figure 4.2: Mechanical strength tests of the fuels (stress-strain graph)

used in the other, including water. The inner diameter of the samples is 40 mm and the outer diameter is 86 mm. As seen in Figure 4.2, the increase in the concentration of binder directly affected the strength properties of the fuel. During the strength test, 300 kN MTS 647 Hydraulic Press was used. All specimens exhibit a similar initial stiffness, as indicated by the linear portion of the stress-strain curves. This linear region represents the elastic deformation where the material returns to its original shape upon unloading. The similar slopes in the elastic region across all specimens suggest that the elastic modulus, which is a measure of stiffness, is not significantly influenced by the binder content. This implies that the elastic properties of the metal matrix are dominant and not substantially altered by varying the binder percentage from 5% to 10%.

Specimens with 10% binder content (Specimens 5 and 6) reach a higher peak stress compared to those with 5% binder (Specimens 1 and 2). The peak stress corresponds to the ultimate compressive strength (UCS) of the material. The higher

UCS in specimens with increased binder content suggests that the binder enhances the load-bearing capacity of the composite material. The additional binder likely improves the cohesion between metal particles, leading to a stronger material capable of withstanding greater forces before failure. This enhanced bonding could also reduce the occurrence of micro-cracks and other stress concentrators within the material.

Specimen 6, which contains 10% binder, shows the highest strain at failure, indicating greater ductility compared to other specimens. The ability to sustain larger deformations before failure is evident in the extended curve beyond the elastic region. Analysis: The increased binder content appears to improve the ductility of the material, particularly in Specimen 6. This suggests that the binder may act as a plasticizer, allowing the material to deform more before fracturing. The enhanced ductility could result from better energy absorption and distribution throughout the material, delaying the onset of fracture.

When we check Post-Peak Behavior (Toughness and Brittle vs. Ductile Failure) we can say Specimens 1 and 2 (5% binder) show a more gradual decline in stress after the peak, indicating some plastic deformation before failure. When we checked the toughness of the produced samples, specimens with 10% binder (particularly Specimen 6) appear to maintain higher stress over a longer strain range, indicating higher toughness. The increased toughness in specimens with 10% binder suggests that these materials can absorb more energy during deformation, which is critical for applications involving dynamic or impact loads. This could be due to the improved bonding and cohesion provided by the higher binder content, which helps in distributing the applied stress more evenly throughout the material.

As seen in Table 4.1, the average toughness of specimens with a 10% binder ratio is approximately 4.96 times higher than that of specimens with a 5% binder ratio. This substantial increase indicates that increasing the binder content significantly enhances the material's energy absorption capacity before failure, thus improving its toughness.

The detailed analysis of the stress-strain curves supports the conclusion that

Specimen	**Binder Ratio (%)**	**Toughness (N/mm^2)**
Specimen 1	5	0.35212
Specimen 3	5	0.34105
Specimen 2	10	1.8701
Specimen 4	10	1.5717
Average (5% Binder)		**0.3466**
Average (10% Binder)		**1.7209**

Table 4.1: Toughness values of specimens with different binder ratios

increasing the binder content from 5% to 10% enhances the tensile strength and ductility of the material, making it more robust under tensile loading.

Relative Error Analysis of Mechanical Strength Test

1. Cross-sectional Area (A):

$$A = \frac{\pi d^2}{4}$$

The relative error in A is:

$$E_A = 2 \cdot \frac{\Delta d}{d}$$

2. Compressive Stress (σ):

$$\sigma = \frac{F}{A}$$

The relative error in σ is:

$$E_\sigma = \sqrt{\left(\frac{\Delta F}{F}\right)^2 + \left(\frac{\Delta A}{A}\right)^2}$$

3. Strain (ϵ):

$$\epsilon = \frac{\Delta h}{h}$$

The relative error in ϵ is:

$$E_\epsilon = \sqrt{\left(\frac{\Delta(\Delta h)}{\Delta h}\right)^2 + \left(\frac{\Delta h}{h}\right)^2}$$

4. Young's Modulus (E):

$$E = \frac{\sigma}{\epsilon}$$

The relative error in E(Young Modulus) is:

$$E_E = \sqrt{\left(\frac{E_\sigma}{\sigma}\right)^2 + \left(\frac{E_\epsilon}{\epsilon}\right)^2}$$

A summary of the relative error is presented in Tab. 4.2.

Quantity	**Value**	**Uncertainty (Δ)**	**Relative Error (%)**	**Source of Uncertainty**
Height of the Specimen (h)	40 mm	$\pm$0.04 mm	0.1	Caliper accuracy
Inner Diameter (d_{in})	40 mm	$\pm$0.04 mm	0.1	Caliper or micrometer accuracy
Outer Diameter (d_{out})	86 mm	$\pm$0.086 mm	0.1	Caliper or micrometer accuracy
Force (F)	1 N $-$ 80,000 N	$1\% \cdot F$	1.0	MTS 647 Hydraulic Press
Displacement (Δh)	1 $-$ 8 mm	$0.2\% \cdot \Delta h$	0.2	Hydraulic press sensor
Cross-sectional Area (A)	4560.23 mm^2	-	0.28	Derived from diameter
Compressive Stress (σ)	17.54 MPa	-	1.04	Force and area uncertainties
Strain (ϵ)	0.05	-	0.22	Displacement and height
Young's Modulus (E)	350.8 MPa	-	1.06	Stress and strain

Table 4.2: Measured parameters, derived quantities, and relative errors in compression test

The relative error analysis conducted for the mechanical strength test demonstrates the reliability and precision of the experimental measurements, with low uncertainties across all calculated parameters. The cross-sectional area and strain showed minimal errors of 0.28% and 0.22%, respectively, confirming the accuracy of dimensional and displacement data. The slightly higher uncertainty in compressive stress and Young's modulus, at 1.04% and 1.06%, respectively, was primarily attributed to the limitations in force measurement precision. These findings indicate that the mechanical properties of the fuel samples, particularly their compressive strength and Young's modulus, were determined with high reliability,

ensuring confidence in the structural performance predictions of the fuel under operational conditions. However, minor variations in the results highlight the influence of measurement precision on the derived properties, suggesting that improvements in instrumentation could further refine the accuracy. The low error levels provide a strong foundation for evaluating the fuel's stability and effectiveness in high-pressure environments.

4.1.2 Thermal Conductivity Estimation Using the Rule of Mixtures with Air Voids

This section presents a methodology for calculating the effective thermal conductivity (k_{eff}) of a metal powder composite containing magnesium, aluminum, sodium silicate, and air voids. The approach uses both series and parallel models as boundary conditions and combines them for a realistic estimate. This method has been validated in prior studies [Doe and Smith, 2021, Brown and Clark, 2024, Zhang and Li, 2023].

Rule of Mixtures for Composite Thermal Conductivity

The Rule of Mixtures estimates the effective thermal conductivity of a composite by considering the contributions of all components based on their volume fractions and individual conductivities. The general formulas are:

$$k_{\text{eff,parallel}} = \sum_{i=1}^{n} V_i \cdot k_i \tag{4.1}$$

$$\frac{1}{k_{\text{eff,series}}} = \sum_{i=1}^{n} \frac{V_i}{k_i} \tag{4.2}$$

where:

- V_i is the volume fraction of component i,
- k_i is the thermal conductivity of component i.

To account for the composite's heterogeneity, the effective thermal conductivity is approximated as the arithmetic mean of the series and parallel models:

$$k_{\text{eff,average}} = \frac{k_{\text{eff,parallel}} + k_{\text{eff,series}}}{2} \tag{4.3}$$

This formula aligns with theoretical and experimental findings in metal powder composites [Doe and Smith, 2021, Brown and Clark, 2024, Zhang and Li, 2023].

Volume Fraction Calculation

The volume fraction of each solid component is calculated as:

$$V_i = \frac{m_i}{\rho_i}$$

where m_i and ρ_i are the mass and density of component i, respectively. The air volume fraction is determined by subtracting the total solid volume (V_{solid}) from the overall sample volume (V_{total}):

$$V_{\text{air}} = V_{\text{total}} - V_{\text{solid}}$$

Thermal Diffusivity and Effective Specific Heat Capacity

The thermal diffusivity (α) and effective specific heat capacity ($c_{p,\text{eff}}$) of the composite are essential for understanding its thermal behavior. These are calculated using the following relations:

$$\alpha = \frac{k_{\text{eff}}}{\rho \cdot c_{p,\text{eff}}} \tag{4.4}$$

$$c_{p,\text{eff}} = \sum_{i=1}^{n} V_i \cdot c_{p,i} \tag{4.5}$$

where:

- $c_{p,i}$ is the specific heat capacity of component i,
- $c_{p,\text{eff}}$ is the effective specific heat capacity of the composite.

Thermal Properties of the Samples

Using the Rule of Mixtures, the effective thermal conductivity (k_{eff}), thermal diffusivity (α), and effective specific heat capacity ($c_{p,\text{eff}}$) were calculated for the samples. The results show that higher density samples exhibit increased thermal conductivity and specific heat capacity due to reduced air voids, while lower density samples demonstrate lower thermal performance.

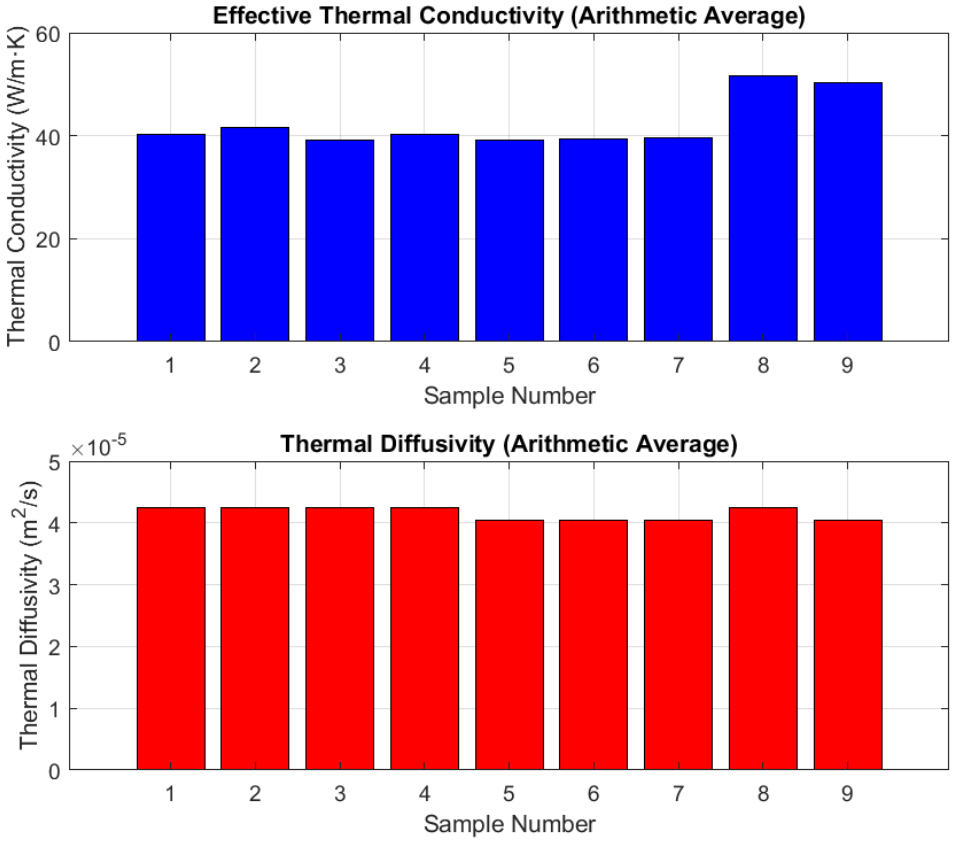

Figure 4.3: Effective Thermal Conductivity (k_{eff}) and Thermal Diffusivity (α) of the Samples.

4.1.3 Igniter Design

In this thesis study, which is based on the use of lunar resources, the ignition system is expected to be obtainable from lunar resources. Therefore, if it is necessary to use

an igniter, it would be logical to use nichrome wire due to its high thermal resistance. Nichrome wires are used in many areas in our daily lives, such as irons, toasters and many other machines. Mechanical properties of Nichrome are presented in Table 4.3.

Table 4.3: Typical properties of nichrome wire (grade: Nichrome 80)

Property	**Value**
Composition	Typically 80% Nickel and 20% Chromium
Melting Point	Approximately 1400°C
Tensile Strength	Around 650 to 1050 MPa
Yield Strength	Around 420 to 720 MPa
Elongation	Approximately 20 to 45% (at room temperature)
Electrical Resistivity	About 1.10 $\mu\Omega \cdot$ m (at 20C)
Thermal Conductivity	Approximately 11.3 W/m·K (at 20°C)
Specific Heat	About 0.460 J/g·°C
Coefficient of Expansion	18 $\times$ 10^{-6} /°C (at 20°C to 1000°C)
Density	Approximately 8.4 g/cm^3

Nichrome wire is placed into the fuel from the inner surface to initiate combustion. Metal-based fuels exhibit ignition challenges, attributed to both the significant thermal conductivity and the substantial evaporation temperatures of metals. A high level of thermal energy must be rapidly transferred to the fuel for ignition. For swift energy transfer, a nichrome wire with 0.8-ohm resistance was utilized, applying a voltage of 36 V. Displayed in the subsequent image is the encapsulation of the fuel alongside the ignition wire post-compaction. The characteristics of the nichrome wire employed for ignition initiation and an image of nichrome wire placed in fuel in the experiments are presented in Table 4.4 and Fig. 4.4, respectively.

Figure 4.4: Fuel with nichrome wire inserted

Properties	Value
Resistance(Ohm)	0.3
Diameter(mm)	1.2
Melting Point(K)	1400
Input Voltage(V)	36 V
Length(mm)	300

Table 4.4: Nichrome wire properties which are used in the tests

Heat transfer analysis of ignition wire to determine oxygen valve opening time

To determine the appropriate ignition delay of the oxygen valve, a transient thermal analysis was conducted using the ANSYS thermal module. This analysis, employing the thermal properties of the fuel obtained in Table 4.3, aimed to model the

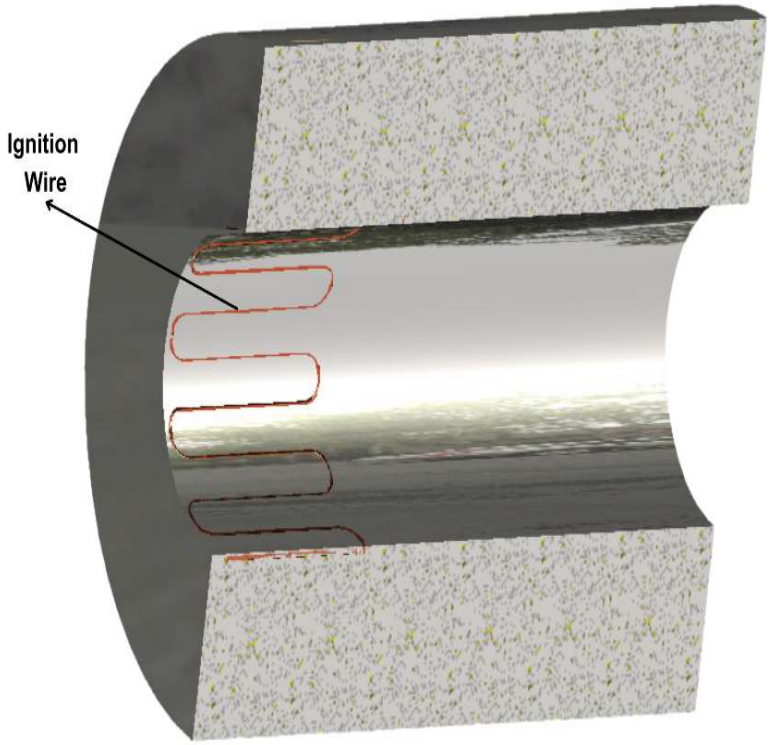

Figure 4.5: Ignitor wire shown in cross-sectional view of fuel

interaction of heat flow from the ignition wire with the fuel and the external environment. The methodology is outlined below: The ignition wire was modeled as a localized heat source, representing the thermal power generated during ignition. This heat was applied as a heat flow boundary condition to the surfaces of the fuel in contact with the wire. The boundary condition was defined using the power value derived from experimental parameters, simulating real-life thermal interactions effectively. The surfaces of the fuel grade in contact with the external environment are determined as adiabatic zerogradient boundary condition is defined. Since very small changes occur on the surfaces in contact with the external environment, using adiabatic boundary conditions or convection boundary conditions does not make a difference in the analyses performed.The thermal properties of the fuel, including thermal conductivity, specific heat capacity, and density, were input based on the results of Table 4.3. Magnesium's ignition temperature was taken as the thresh-

old to determine the ignition point, ensuring that the analysis reflects real-world conditions.

To achieve high accuracy in thermal gradient calculations:

- A global mesh size of 0.5 mm was used throughout the model for uniform resolution.
- The surfaces in contact with the ignition wire were assigned a finer face mesh size of 0.01 mm, capturing the intense localized heating effects near the heat source.

Simulation Setup and Execution The analysis was performed in the Ansys Transient Thermal Module, allowing the temperature evolution over time to be monitored. The solver was configured with the following:

1. Time Step Control: Adaptive time-stepping was utilized to maintain stability and high resolution, particularly around the ignition event.
2. Solution Settings: Material properties and boundary conditions were applied systematically to ensure the accuracy of the results.

The analysis aimed to determine the time at which the maximum temperature of the system reaches magnesium's ignition point. By tracking the evolution of temperature in the fuel:

- The ignition time was identified for each fuel sample.
- These ignition times were used to establish the optimal opening duration for the oxygen valve, with the results presented in Fig. 4.6.

In addition, to understand whether the mesh size is converging, a converge graph between 5 mm and 0.1 mm was drawn and presented in Fig. 28. As can be seen, it converged starting from 0.5 mm mesh size.

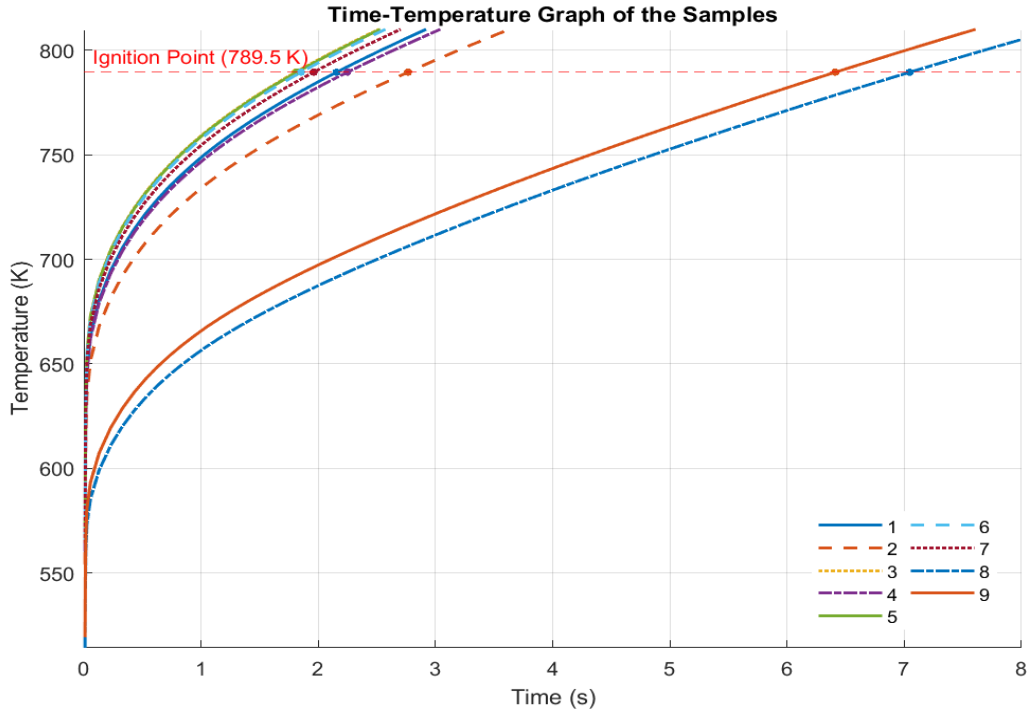

Figure 4.6: Temp-Time graph of the fuel samples

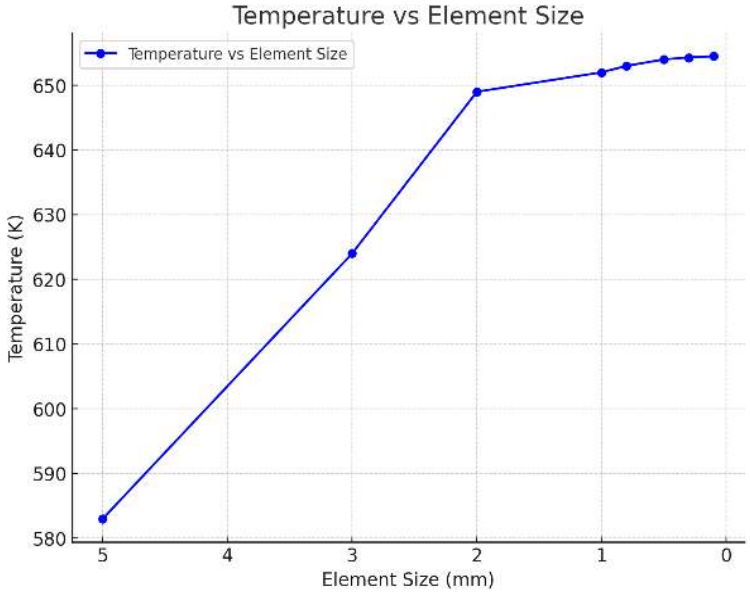

Figure 4.7: Element size vs temperature convergence

Magnesium powder particles exhibit a significantly lower ignition temperature compared to bulk magnesium. For fine magnesium powders with a particle size of 44 µm, ignition can occur at temperatures as low as 789.5 K (516.35°C) [Kim et al., 2022]. This lowered ignition threshold is due to the increased surface area-to-volume ratio of the particles, which promotes enhanced reactivity and facilitates rapid oxidation. Thermal analysis of fuel samples, considering the thermal properties of the materials and ignition temperature, reveals that fuel samples compressed at 100 bar ignite before reaching the 3-second mark, as illustrated in Graph 4.6. Furthermore, samples created with 10% binder (Samples 5, 6, 7) tend to ignite slightly faster than those containing 5% binder (Samples 1, 2, 3, 4). On the other hand, samples compressed at 150 bar exhibit ignition times exceeding 6 seconds. Based on this analysis, it is recommended to open the oxygen valve at the 3-second mark for fuels pressed at 100 bar.

4.2 Test Setup and Motor Design

The design of the engine on which the tests were carried out is presented in Fig. 4.8. The engine is made of stainless steel 316 with external structure. In order to minimize structural damage, the safety coefficient is set around 7-8 times the engine operating pressure. The combustion chamber is isolated from the engine structure using the phenolic tube. Graphite was used in the nozzle, post-combustion chamber and pre-combustion chamber parts. It was first thought to connect the connection cables of the nichrome wire placed in the fuel to the combustion chamber by inserting it through the nozzle, but in some tests, it was seen that this cable could momentarily cause problems in the stability of the combustion chamber and it was connected to the fuel through the pre-combustion chamber with the help of a part connected to the engine.

In the test setup, a manual ball valve was used at the oxygen tank outlet for safety reasons. Solenoid valves were provided by SMSTork company. Pressure reading electronic systems were provided by NI company. Pressure transducers recorded data at high frequency during the combustion period. Additionally, National Instruments

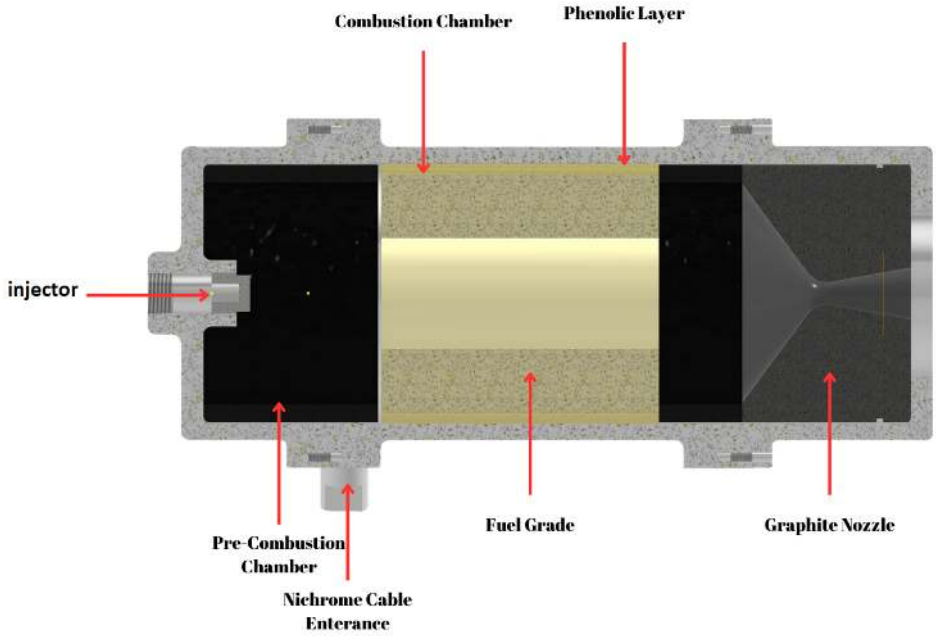

Figure 4.8: Engine design

DAQ was used as the data reading system. The ready version of the pre-ignition setup is presented in Figure 4.9. In all supply conduits, as well as immediately preceding the motor inlet, check valves are installed. Pressure and temperature data acquisition is carried out using a system by National Instruments and software known as Lab View Signal Express. The DAQ system's sampling frequency is configured to 5.12 kHz. All connections, including those for ball valves, relief valves, and check valves, are procured from Hamlet. Meanwhile, the pressure transducers are obtained from IFM electronics. The plumbing, fittings, and piping within the testing apparatus are of a 3/8-inch size, and the pressure transducers are compatible with a 1/4-inch NPT connection.

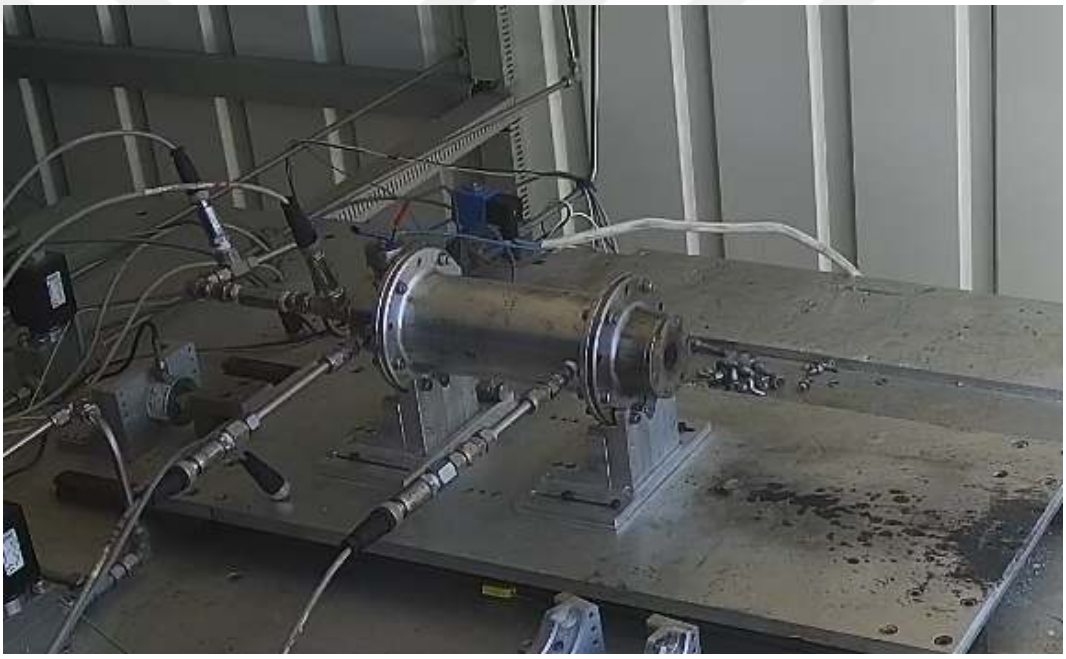

Figure 4.9: Test setup

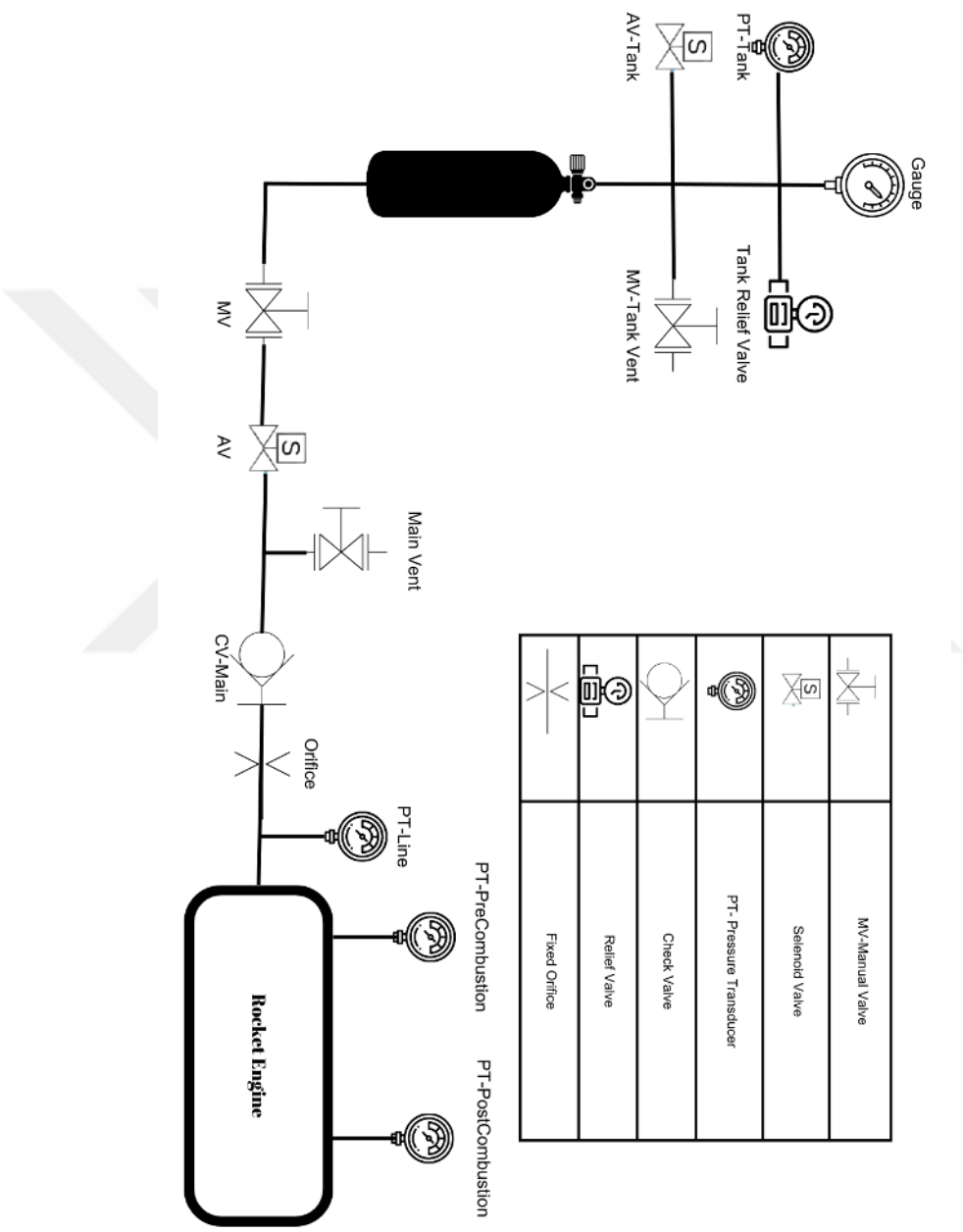

Figure 4.10: P&ID Design of the test setup

A 1.2 mm diameter orifice was used to ensure the oxidizer flow rate reached choked conditions during the test. In choked flow, the downstream pressure does not affect the flow rate, as the velocity of the gas at the orifice throat reaches the speed of sound. The following choked flow equation was used to determine the flow rate:

$$\dot{m} = C_d A_o P_1 \sqrt{\frac{\gamma}{RT_1} \left(\frac{2}{\gamma+1}\right)^{\frac{\gamma+1}{\gamma-1}}} \tag{4.6}$$

- $\dot{m}$: mass flow rate, measured in kilograms per second (kg/s)
- C_d: discharge coefficient, a dimensionless number
- A_o: area of the orifice, measured in square meters (m^2)
- γ: specific heat ratio (adiabatic index), dimensionless ($\gamma = \frac{C_p}{C_v}$)
- P_1: upstream pressure, measured in Pascals (Pa)
- R: specific gas constant, measured in joules per kilogram per kelvin (J/kg·K)
- T_1: upstream temperature, measured in Kelvin (K)

The ratio of downstream pressure to upstream pressure (P_2/P_1) was ensured to be less than the critical pressure ratio:

$$\frac{P_2}{P_1} < \left(\frac{2}{\gamma+1}\right)^{\frac{\gamma}{\gamma-1}} \tag{4.7}$$

to guarantee choked flow conditions. The discharge coefficient (C_d) was determined to be 0.90 based on flow tests conducted with water. While C_d can vary with fluid properties, studies have shown that for sharp-edged orifices operating under choked flow conditions, it remains relatively consistent across different fluids, including gases [Miller, 1996]. Therefore, the C_d value obtained from water tests was used as a reference for gaseous oxygen flow in this study.

4.3 Manufacturing and Testing Costs

The cost analysis for the testing process has been simplified to represent an average cost per test. This cost includes both consumable materials and reusable components required for each test cycle. Based on the materials used, the average cost per test is calculated as 866.18 USD. This value accounts for the expenses associated with consumable items, such as magnesium and aluminium powders, phenolic layers, graphite nozzles, and other expendable components. Additional reusable equipment costs are excluded from this figure as they are amortized over multiple test cycles. All other infrastructure and equipment, including data acquisition systems, pressure transmitters, and safety setups, were provided externally and are not included in the per-test cost calculation.

Chapter 5

TESTS AND RESULTS

5.1 Test Classifications and Procedures

Two different fuel types were used in the tests, differentiated by their binder content: one fuel type contained 10% binder, while the other contained 5%. The purpose of these tests was twofold: to evaluate the stability of the engine during combustion and to assess how the varying binder content affected the mechanical and combustion properties of the fuel. Specifically, the study examined the influence of binder ratio on factors such as combustion efficiency, the structural integrity of the fuel, and the stability of pressure and regression rates within the engine.

The testing procedure works as follows. First of all, the indicator of the gas oxygen tank is adjusted for a certain pressure for the calculated flow rate. Afterward, the ball valve is opened and the line is pressurized. After the line is pressurized, the ignition system is activated and the pressures are checked using pressure reading software. When the ignition button is pressed, the system automatically starts testing in a certain cycle. The timing of the cycle is presented in Fig. 5.1.

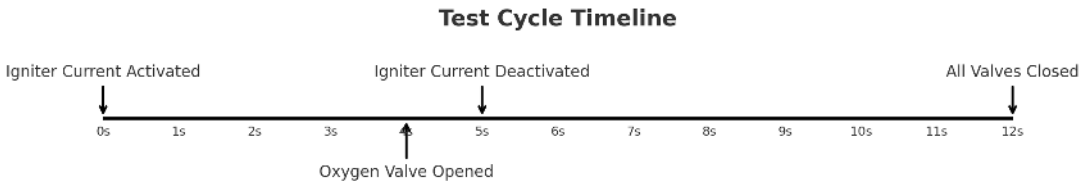

Figure 5.1: Test cycle

The tests last 12 seconds in total and oxygen is supplied to the combustion chamber for 8 seconds. The reason for the 5-second lead in the current given to the

ignition wire compared to the valve opening is to prevent the cooling effect of the oxygen gas flow on the nichrome wire.

5.2 Igniter Tests

To test the ignition system, the igniter placed in the fuel was tested in the ambient environment before being placed in the engine. While performing these tests, it was thought that the pressing pressure of the fuel may affect the initiation of combustion. The high pressing pressure during the production of the fuel increases the density of the fuel and also increases the thermal conductivity. Therefore, before the igniter can raise the fuel to ignition temperature, it may cause all the fuel to melt leading to a failed ignition.

In the igniter tests, it was seen that the fuels tested at 100 bar pressure, due to the high thermal conductivity, the ignition wire cannot instantly increase the surface temperature to the combustion temperature, therefore ignition does not occur. As the duration of the applied current increases, non-uniform temperature increases occur in areas where the ignition wire has little contact with the fuel the wire melts and the ignition does not occur. An image of the test performed is presented in Fig. 5.2. As can be seen, although burning started locally at some points, the burning in those areas stopped after a while and did not progress due to the high thermal conductivity.

On the other hand, when this test is performed with fuel pressed at 100 bar, it is seen that the fuel is ignited. The number of voids in the fuel is important for the ignitability of the fuel. Figure 5.3 shows the ignition moment of 100 bar pressed fuel.

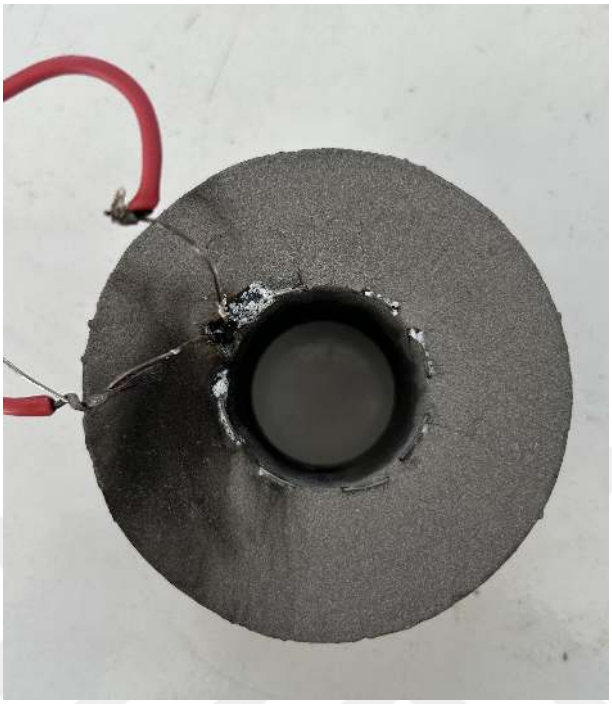

Figure 5.2: Igniter test fail of 150 bar pressed fuel composition

Figure 5.3: Igniter test of 100 bar pressed fuel composition

5.3 Tests of The Engine

A total of 9 tests were conducted, and ignition did not occur in the tests performed with fuel samples 8 and 9. The reason why ignition did not occur is that the heat generated by the ignition wire was rapidly dissipated within the fuel due to its high thermal conductivity. This caused the fuel to take a longer time to reach the ignition temperature. Additionally, during the manufacturing process, the ignition wire was partially exposed to air at certain points where it made contact with the inner surface of the fuel. This exposure caused localized overheating of the nichrome wire, exceeding its melting point, which led to wire breakage at these locations. As a result, the ignition system failed to adequately heat the fuel to the required temperature, leading to unsuccessful tests with these fuel samples. The tests performed and their information are presented in Table 5.1.

Sample No	**Mass of Fuel (g)**	P_{up} **(bar)**	$\dot{m}_{ox}$ **(g/s)**	**Density (kg/m³)**	**Test Status**
1	477.288	30.1	7.6	947	Success
2	470.232	29.9	8.65	933	Success
3	463.68	33.1	8.1	920	Success
4	489.888	33.4	8.46	972	Success
5	483.336	34.1	8.79	959	Success
6	491.904	34.9	8.89	976	Success
7	497.405	37.4	9.13	983	Success
8	613.368	-	-	1217	Ignition Fail
9	629.496	-	-	1249	Ignition Fail

Table 5.1: Test Details

A new nozzle was used after each test to avoid affecting the results, thus ensuring that burnt metal products adhering to the nozzle or erosion occurring in the nozzle throat did not affect the test results.

5.3.1 Results of Tests Containing 5% Binder by Mass

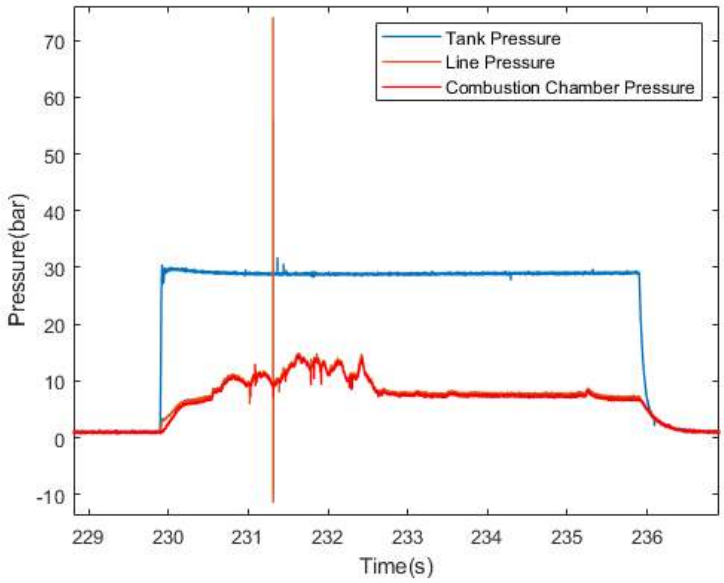

Figure 5.4: Test of sample No 1 (m_{ox}=7.6 g/s, 5% Binder, 100 Bar press pressure)

This test with sample 1 was performed for 6 seconds. It can be seen that there are many stable oscillations in the first half of the test. These unstable conditions were also observed in the video footage of the test. After the first half of the test, the combustion chamber pressure remained below 10 bar again and some oscillations of small magnitude continued to be observed, but it still remained partially stable. A change in pressure above 70 bar was observed in miliseconds. This sudden change in line pressure may be caused by particles breaking away from the fuel suddenly clogging the nozzle. However, as a result, it can be said that a more stable combustion was observed after the 3rd second of the test, even though it did not reach the design pressure which is 15 bar.

The graph of the test performed with Fuel Sample 2 is presented in Figure 5.5. In this test, which is partially similar to the burn test number 1, although the tank pressure was about 34 bar, the combustion chamber pressure could not reach 10 bar.

However, when compared to the fuel sample number 1 with 5% binder, the pressure increased steadily from the 3rd second of the test and reached up to 9.2 bar. In this test, it was observed that the combustion chamber pressure remained at low levels in general and did not reach the desired value of 15 bar.

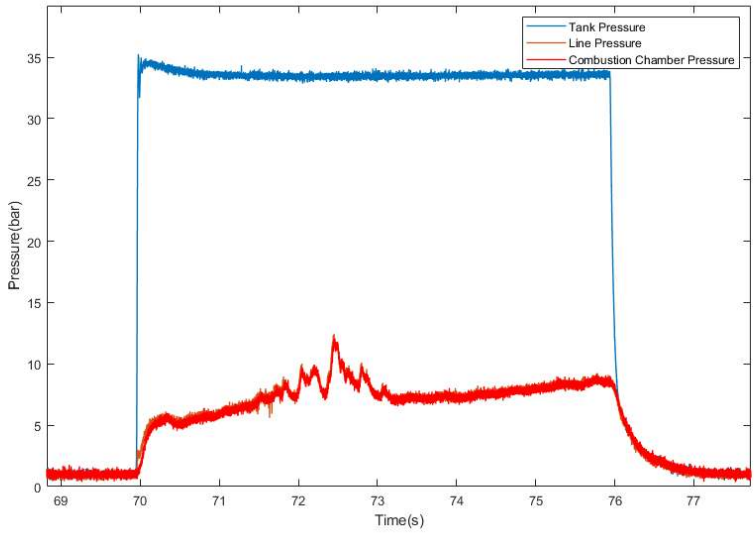

Figure 5.5: Test of sample No 2 (m_{ox}=8.65 g/s , 5% Binder, 100 Bar press pressure)

When we examine the test graph of fuel sample no 3, we see some instabilities above 20 bars, similar to fuel sample number 1. Sudden changes in the tank pressure and in the combustion chamber are indicators of momentary blockages in the nozzle due to nearby parts breaking off. In this test, unlike the previous test, a sudden increase in pressure occurs at the 7th second of the test. Although the combustion chamber reaches a stable operating state from the 3rd second of the test, this increase that occurs in the following periods is one of the clear indicators of the problem in the close formation. Even when combustion reaches a stable state, the combustion chamber pressure remains below 10 bar. This sudden change in line pressure indicates that the check valve is momentarily closed. This shows that clogging has occurred in the nozzle chamber over a significant period of time.

The test performed with sample number 4 was carried out with a slightly higher oxidizer mass flow rate. Tank pressure was determined as 33.5 bar. However, a

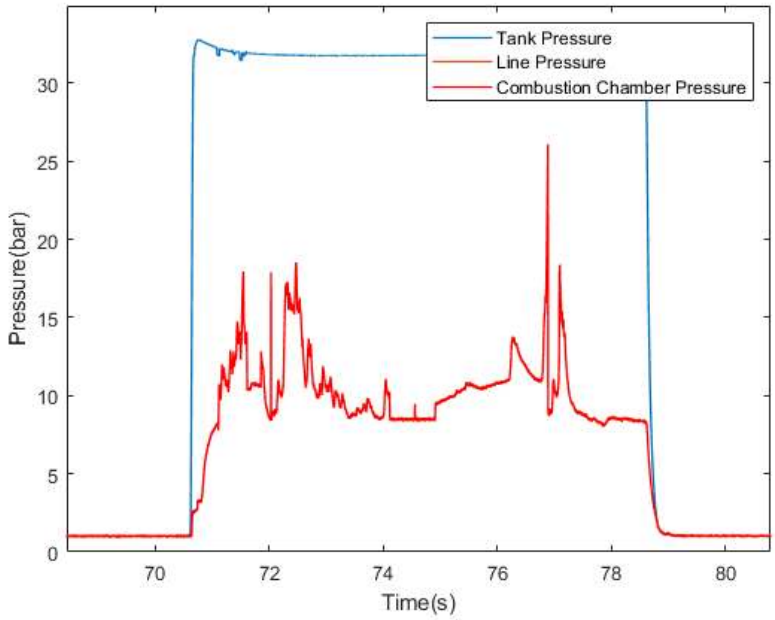

Figure 5.6: Test of sample No 3 (m_{ox}=8.1 g/s, 5% Binder, 100 Bar press pressure)

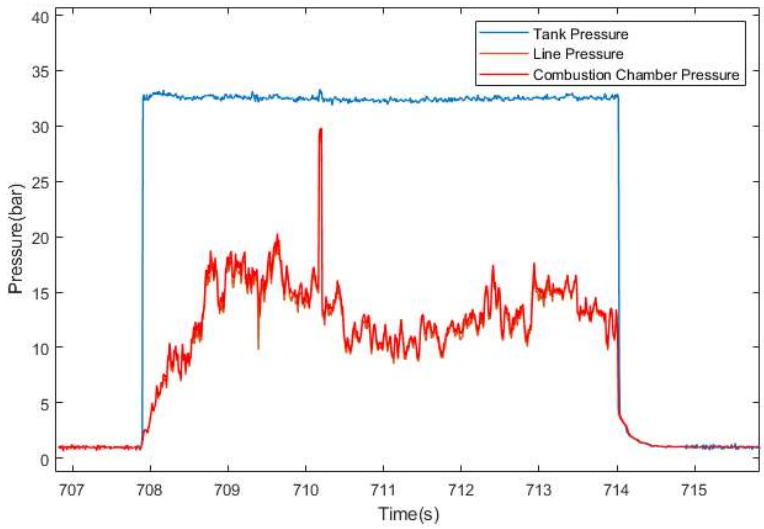

Figure 5.7: Test of Sample No 4 (m_{ox}=8.46 g/s, 5% Binder, 100 Bar press pressure)

stable combustion zone could not be achieved during this test. So much so that this test was a test with much more oscillations compared to other tests. Although the oscillation rate was high, the magnitude of the oscillations during the test was

slightly smaller than in other tests. Additionally, in the test performed with Sample no 4, the average combustion chamber pressure was observed to be higher. It can be said that in the test carried out with Fuel No 4, serious blockages occurred in the nozzle and therefore unexpected pressure increases occurred. In the observations made after the test, it was observed that too much combustion products adhered to the nozzle surface.

5.3.2 Results of Tests Containing 10% Binder by Mass

The pressure values for the test conducted with fuel sample 5 (%10 binder by mass) are presented in Figure 5.8. During this test, the combustion chamber pressure was initially low but gradually increased, reaching approximately 14 bar in the latter half of the test and demonstrating stable combustion. This stability indicates that the transition zone between the fuel and oxidizer in the combustion chamber successfully achieved equilibrium, allowing the system to operate near the design pressure.

The tank pressure readings showed minor oscillations, which were determined to be electronic in nature and unrelated to the combustion dynamics. These variations do not affect the overall stability or performance of the combustion chamber. The propellant setting in the gaseous oxygen (GOX) system ensured proper oxidizer flow, contributing to the consistent combustion observed in the test results.

The pressure values of the other test performed with fuel sample no. 6 are presented in Figure 5.9. When this test chart is examined, as in sample 5, the combustion chamber pressure increases halfway through the test and some oscillations are observed. After half of the test, it is seen that there is a stable combustion again. When compared to fuels with 5% binder additives, it is seen that the oscillation magnitude values are lower. Especially in this test, we see a much more stable pressure graph starting from the 3rd second of the test. Similar to sample number 4, the pressure is around 13 bar in the 3rd second of the test, but it shows a certain increase and approaches 15 bar at the end of the test which is the targeted pressure in combustion chamber.

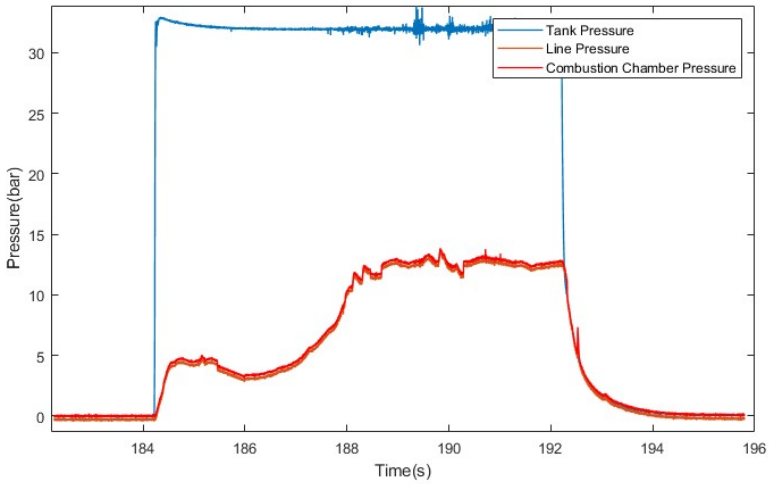

Figure 5.8: Test of sample No 5 (m_{ox}=8.79 g/s, 10% Binder, 100 Bar press pressure)

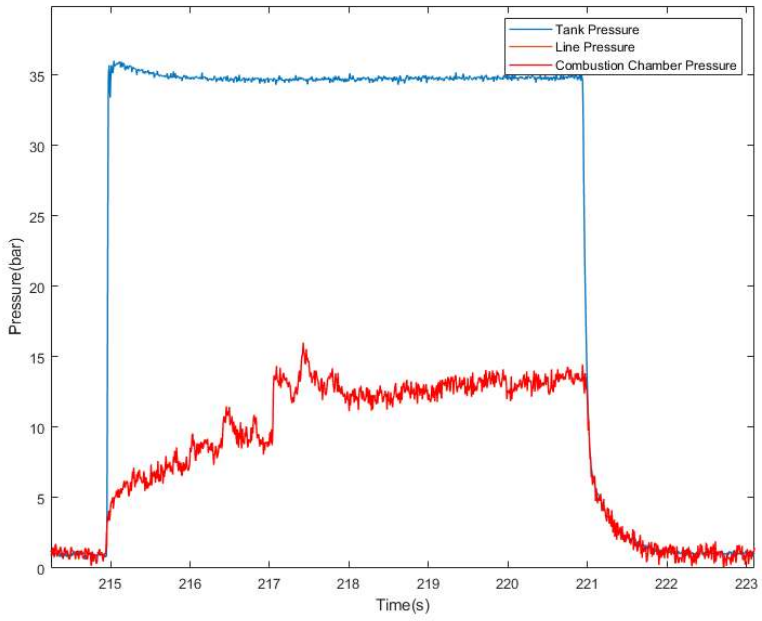

Figure 5.9: Test of sample No 6 (m_{ox}=8.89 g/s, 10% Binder, 100 Bar press pressure)

When the test pressure data performed with fuel number 7 is examined in Fig 5.10, it is clearly seen that there is an ignition delay(the delay in the engine reaching or exceeding its design pressure). In this test, which was carried out at a slightly

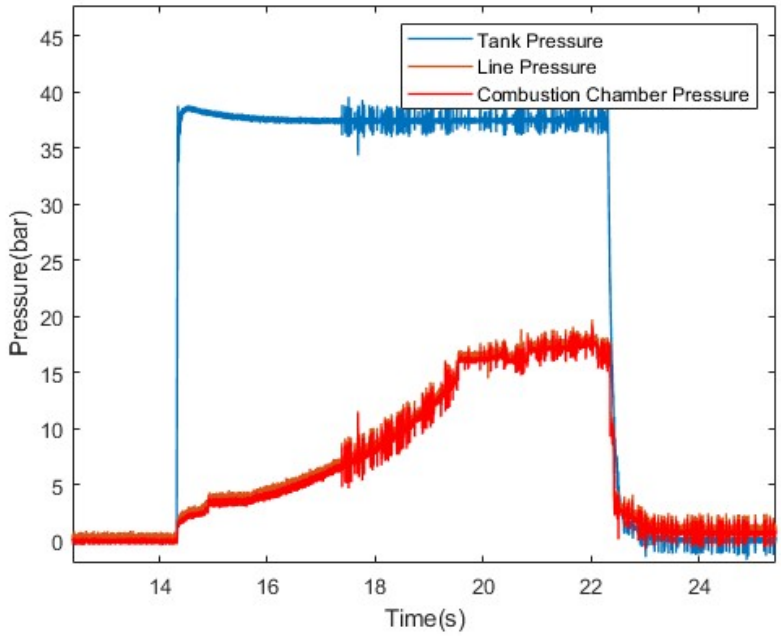

Figure 5.10: Test of sample No 7 (m_{ox}=9.13 g/s, 10% Binder, 100 Bar press pressure), $P_d = 15$ bar

higher oxidizer flow rate compared to other tests, the combustion chamber pressure reached around 18 bar towards the end of the test.

5.4 Evaluation of test results and conclusion

5.4.1 Post-Test Analysis of Combustion Chamber and Fuel Residues

When the 7 tests were evaluated, it was seen that the oscillation magnitudes were much higher, especially in the tests containing 5% binder. Both the inadequate structural integrity of the fuel and the differences that occurred during fuel production caused different pressure graphs to be read in the tests. Both negative and positive oscillations exceeding 30 bars were observed during tests in both the pressure line and the combustion chamber. These pressure fluctuations are the biggest sign that the combustion chamber does not meet the design criteria and that the combustion stability is inadequate. The photo of the inner surface of the nozzle after the test with sample number 3 is presented in Figure 5.11. Also for comparison, a

visual of the nozzle of sample 6 after the test with 10% binder is presented in Figure 5.11.

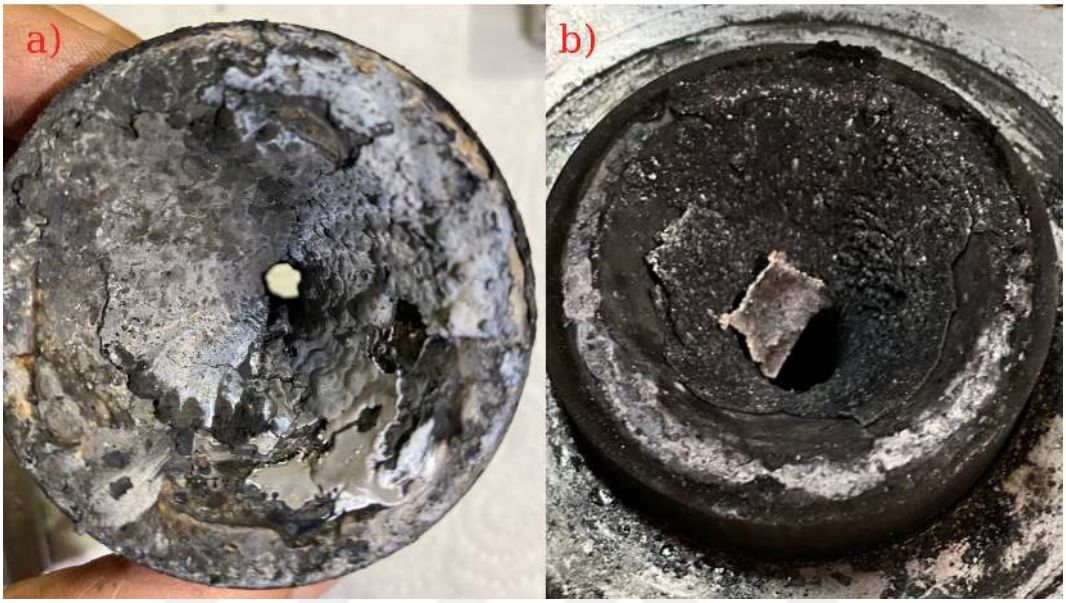

Figure 5.11: Nozzle inner surface of a) Sample 3 (5% Binder) b) Sample 6 (10% Binder)

During the test of Sample 3, which was prepared using 5% binder, it was observed that a non-uniform layer with varying thicknesses formed on the inner surface of the nozzle. This layer ranged from 0.8 mm to 3.6 mm in thickness and resulted from incomplete combustion by-products detaching from the fuel and adhering to the nozzle surface. The non-uniformity of the layer suggests that the combustion by-products were not uniformly distributed or fully vaporized. The irregularity in the layer's formation can be attributed to insufficient combustion time for the fuel particles to fully react. The heat generated by the combustion process was rapidly conducted away from the reaction zone, preventing the fuel from reaching its optimal burning temperature. This issue was compounded by the fact that some portions of the combustion by-products adhered to the nozzle before reaching their boiling point, leading to the observed uneven deposition. Additionally, considering the results of the structural compression tests conducted on the fuel, it can be inferred that large fragments detaching from the fuel instantaneously during combustion may

also contribute to the formation of the non-uniform layer on the inner nozzle surface. Moreover, this thick layer observed on the nozzle surface aligns with the pressure data obtained during the test. Analysis of the pressure-time graph suggests that the rapid detachment of fuel particles and their incomplete combustion contributed to significant variations in pressure. These factors emphasize the importance of optimizing combustion conditions to ensure complete vaporization of the by-products, thus preventing such depositions and improving overall engine performance.

In contrast, the test of Sample 6, prepared using 10% binder, resulted in the formation of a much thinner layer on the nozzle's inner surface. Measurements indicated that this layer's thickness ranged between 0.5 mm and 1.1 mm. The reduced thickness suggests improved combustion characteristics and reduced deposition, likely due to the increased binder content. The higher binder content may contribute to more efficient combustion by enhancing the fuel's structural stability and allowing for a more uniform burn. This increased efficiency could potentially lead to higher localized combustion temperatures, reducing the accumulation of incomplete combustion by-products on the nozzle surface.

When comparing these two samples, it is evident that the nozzle deposits in the 5% binder case not only exhibited greater thickness but also correlated with significant oscillations in the pressure sensors. These oscillations suggest the presence of liquid-phase combustion products either lingering in the combustion chamber or adhering to the nozzle surface. This behavior could result from combustion products failing to reach the boiling point and remaining in a liquid state, contributing to instability in the combustion process. Visual inspection further confirmed these observations, highlighting a dense layer of liquid-phase by-products on the nozzle surface in the 5% binder case.

Visuals of the combustion chamber interiors after both tests are presented in Fig. 5.12. Detailed inspections of the inner surface of the combustion chamber revealed notable differences between the tests conducted with 5% and 10% binder ratios.

For the tests conducted with 5% binder (Sample 3), it was observed that the fuel residue remained within the combustion chamber at varying thickness levels.

Figure 5.12: Combustion chamber after test of a) Sample 3(5% Binder) b) Sample 6(10% Binder)

When an attempt was made to remove the fuel residue, it completely disintegrated into fragments. Additionally, partial burning of the phenolic insulator was noted, along with further fragmentation of the fuel during the removal process. This indicates incomplete combustion and structural instability of the fuel under the test conditions.

In contrast, the test conducted with 10% binder (Sample 6) displayed significantly improved combustion characteristics. Compared to the 5% binder sample, the combustion in the 10% binder sample appeared more uniform and consistent across the entire surface of the fuel. The fuel residue was successfully removed from the combustion chamber without disintegration, demonstrating better structural integrity. The extracted fuel sample is presented in Fig. 5.13.

5.4.2 FFT of the Sample 7's Test Result

During the test conducted with Sample 7, a steady increase in combustion chamber pressure up to 18 bar was observed over a duration of 5 seconds. However, starting around the 4th second of the test, an instability was detected. Notably,

Figure 5.13: Sample 6 fuel Grade after the test

this instability did not originate from the combustion chamber itself. It is likely that this instability was caused by the electronic data logging system or sensors. The issue began around the 4th second and persisted in the tank pressure, combustion chamber pressure, and line pressure, even after the oxygen valve was closed. These oscillations continued after the conclusion of the test and were determined not to stem from combustion stability. This conclusion was supported by FFT (Fast Fourier Transform) analysis conducted on the data collected during and after the test. The results of the FFT analysis are presented in Fig. 5.14.

As shown in Fig. 5.14, the frequencies and amplitudes of the sampled data during and after the test are remarkably similar. This observation further confirms that the oscillations did not originate from the combustion chamber but were instead caused by the electronic measurement systems. These observations underscore the impact of binder ratio on combustion uniformity, structural stability, and post-test fuel handling, with the 10% binder sample exhibiting superior performance.

5.4.3 Regression Rate and Combustion Efficiency Analysis

The regression rate can be calculated as space-time averaged using the equation below.

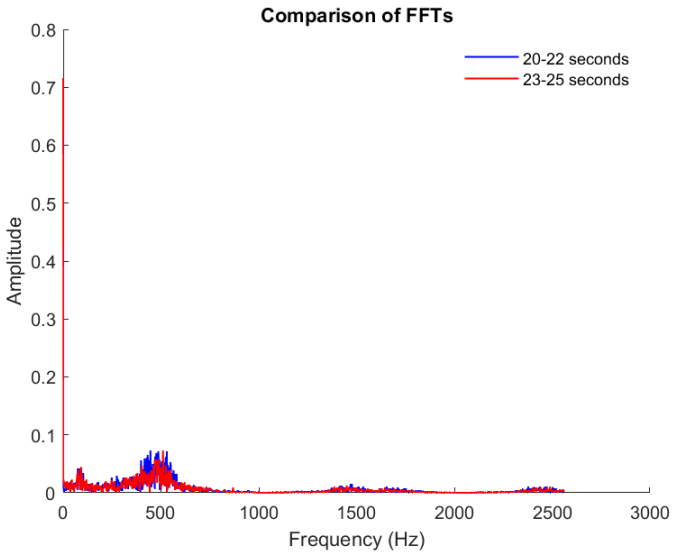

Figure 5.14: FFT analysis of the Sample 7's Test

$$\dot{\overline{r}} = \frac{r_f - r_0}{t_b} \tag{5.1}$$

To calculate the combustion chamber efficiency, the average pressure values of the combustion chamber were taken and the c^*_{exp} value obtained from these values was used. The equation used for the efficiency calculation is presented below. To calculate the combustion chamber efficiency, the average pressure values of the combustion chamber were taken and the c^*_{exp} value obtained from these values was calculated. The combustion chamber efficiency was calculated by comparing the c^*_{exp} value obtained from the experimental results with c^*_{theo}. The equations used in the calculations are presented below.

$$c^*_{\text{exp}} = \frac{\overline{P}_{ch} A_{th}}{\dot{m}_{ox} + \dot{m}_f} \tag{5.2}$$

$$\eta_{\text{comb}} = \frac{c^*_{\text{exp}}}{c^*_{\text{theo}}} \tag{5.3}$$

$$A_{\text{th}} = \pi \frac{d_{\text{th}}^2}{4} \tag{5.4}$$

In order to avoid any structural damage, it was requested that not all of the fuel burn during the tests. For these reasons, although the initial radius r_0 was the same in all tests, the radius r_f was different in all tests. Since there are significant differences in the formation of the fuel after combustion, r_f was calculated by taking into account the post-burning weight of the fuel, and an equivalent r_f radius was obtained.

Sample No	O/F	$m_{ox}(g/s)$	$t_b(s)$	$\bar{r}(mm/s)$	$G_{ox}(k\bar{g}/m^2.s)$	η_{comb}
1	0.43	7.6	6	1.251	4.289	0.488
2	0.41	8.65	8	1.495	4.081	0.461
3	0.44	8.10	8	1.270	4.103	0.530
4	0.40	8.46	6	1.397	4.603	0.545
5	0.36	8.79	6	1.629	4.519	0.407
6	0.39	8.89	6	1.515	4.699	0.411
7	0.38	9.13	8	1.495	4.304	0.421

Table 5.2: Regression rates and oxidizer mass fluxes

In general, the data obtained from the tests demonstrate that such an engine can be functionalized effectively. However, certain side conditions need to be carefully examined to ensure optimal performance and reliability. One critical issue is the potential for catastrophic problems in the engine structure due to the high temperatures reached by the combustion chamber. While the implementation of a regenerative cooling system could enable longer test durations, an alternative approach would be to use thicker insulation around the combustion chamber. This could provide a simpler and more cost-effective solution to mitigate thermal stress and maintain structural integrity. The formula used to calculate the average oxidizer mass flux is presented below.

$$\overline{G_0} = \frac{4 \cdot \dot{m}_0}{\pi \cdot (r_0 + r_f)^2}$$

When the combustion chamber efficiencies obtained were examined, it was seen that the combustion chamber efficiency was 30% lower in the tests conducted using 10% binder compared to the tests conducted using 5% binder, but it was observed that the combustion chamber pressure approached the combustion chamber design pressure and was more stable from the first half of the test conducted with 10% binder. The increase in the combustion chamber pressure was more delayed. This may be due to the difference in the thermal conductivity in the fuel or other reasons, which may cause the combustion chamber temperature to reach the temperature that will vaporize the combustion chamber products later. This situation could also be determined when the test images were examined. When the test images presented

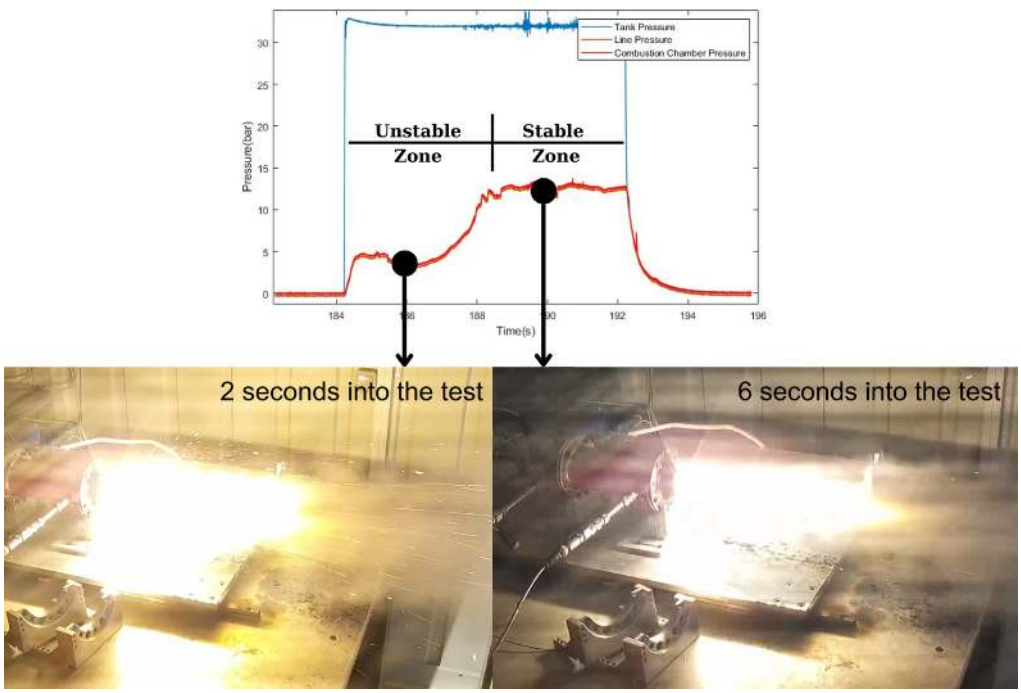

Figure 5.15: Images of the test with %10 binder

in Figure 5.15 are examined, it is very easy to see in the image that the combustion products coming out of the nozzle are in liquid form at the 2nd second of the test.

This is an indication that the combustion products leaving the combustion chamber are still in liquid form at the end of the nozzle. However, when the image from the 6th second of the same test is examined, it is seen that there are much fewer combustion products in liquid form. The increase in the pressure in the graph after the 4th second of the test is an indication that the combustion products contribute to the pressurization of the combustion chamber, and the reason for this is that the combustion chamber reaches the temperature that will vaporize the combustion products. In tests using 10% binder, combustion efficiencies reach much better values when combustion delay is eliminated, and efficiency calculations are made starting from the 5th second of the test. Table 5.3 shows that the combustion chamber efficiency is significantly higher, in the tests conducted with fuel numbers 5, 6, and 7, where ignition delay is dominant.

Sample No	η_{comb}	η_{comb} (without ignition delay)	Differences (%)
5	0.407	0.560	+37
6	0.411	0.592	+43
7	0.421	0.635	+50

Table 5.3: Combustion efficiency comparison

When the mass flux vs regression rate presented by Karabeyoglu et al. [Karabeyoglu et al., 2005a] based on hybrid rocket engine tests performed with pentane using liquid layer theory predictions are examined and the values are compared in Table 5.4.3, it is seen that the regression rate is much higher for the same mass flux values in metal fueled engine the test. This may provide a new perspective on regression rate and mass flux comparisons in metal-fueled hybrid rocket engines.

When analyzing oxidizer flux rates, it is evident that hybrid rocket motors utilizing metal-based fuels demonstrate significantly lower values compared to those using conventional paraffin-based fuels. As shown in Fig. 4.1, metal-fueled hybrid rocket motors perform optimally at much lower oxidizer-to-fuel (O/F) ratios [Karabeyoglu et al., 2005b]. This observation aligns with expectations since metal fuels inherently

exhibit unique combustion characteristics that favor low oxidizer flow conditions. However, the reduced oxidizer flux rates can be further explained by considering the thermal and physical properties of metal fuels. For instance, Fig. 5.17 illustrates that the melt layer thickness in metal-fueled rockets is substantially greater than in classical paraffin-based systems. This increased melt layer thickness results from the high thermal conductivity of metal fuels, which facilitates rapid heat transfer from the combustion chamber to the fuel.

The interplay of these factors—low O/F ratios and enhanced melt layer thickness—explains why metal-fueled hybrid rocket motors exhibit unique combustion dynamics. The high regression rates ($\dot{r}_{fuel}$) of the fuel significantly lower the O/F ratio. These observations are consistent with findings in the literature, such as those reported by Karabeyoğlu et al. [Karabeyoglu et al., 2005b] and Drewniak et al. [Drewniak et al., 2022a], which emphasize the role of thermal conductivity, oxide formation, and viscosity in influencing the combustion behavior of hybrid rocket fuels.

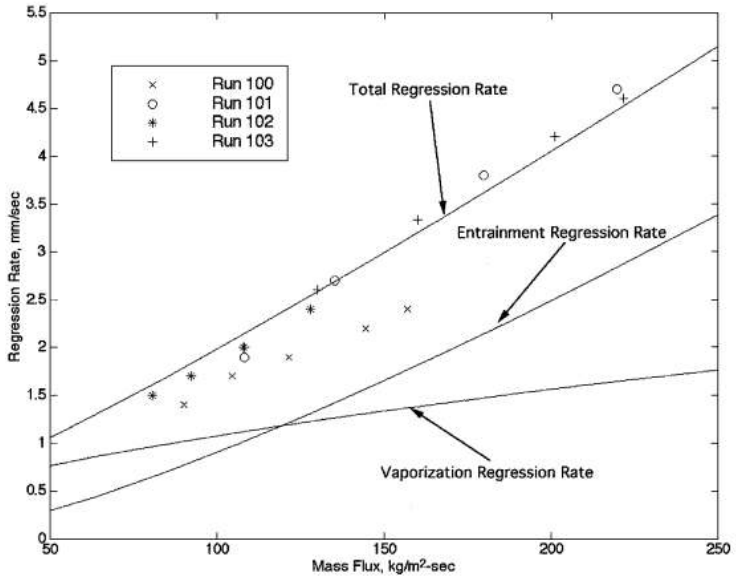

Figure 5.16: Estimations of regression rate vs mass flux Pentane-fueled hybrid rocket engine tests using liquid layer theory [Karabeyoglu et al., 2002]

Methodology for Melt Layer Thickness Calculation

This subsection details the methodology used to calculate the melt layer thickness for liquefying hybrid propellants.

Thermal Thickness Calculation

The thermal thickness (δ_l) is calculated using the following relation:

$$\delta_l = \frac{\kappa_l \rho_l}{\dot{r} \rho_s}, \tag{5.5}$$

where:

- κ_l: Thermal Diffusivity of the liquid phase (m^2/s),
- ρ_l: Density of the liquid phase ($\mathrm{kg/m^3}$),
- $\dot{r}$: Regression rate (m/s),
- ρ_s: Density of the solid phase ($\mathrm{kg/m^3}$).

In the calculation of thermal conductivities, the data obtained from the rule of mixture in the section where the fuel properties were determined were used.

Latent Heat of Melting (L_m)

The latent heat of melting for the composite propellant is computed as a weighted average of the constituents:

$$L_m = f_{\mathrm{Mg}} L_{m,\mathrm{Mg}} + f_{\mathrm{Al}} L_{m,\mathrm{Al}} + f_{\mathrm{Na_2SiO_3}} L_{m,\mathrm{Na_2SiO_3}}, \tag{5.6}$$

where:

- $f_{\mathrm{Mg}}, f_{\mathrm{Al}}, f_{\mathrm{Na_2SiO_3}}$: Normalized volume fractions of magnesium, aluminum, and sodium silicate, respectively,
- $L_{m,\mathrm{Mg}}, L_{m,\mathrm{Al}}, L_{m,\mathrm{Na_2SiO_3}}$: Latent heat of melting for magnesium, aluminum, and sodium silicate (kJ/kg).

Melt Layer Thickness Calculation

The melt layer thickness (h) is determined by combining the thermal thickness and energy considerations:

$$h = \delta_l \ln\left(1 + \frac{C_l \Delta T_l}{L_m + C_s \Delta T_2}\right), \tag{5.7}$$

where:

- C_l: Specific heat capacity of the liquid (kJ/kg·K),
- C_s: Specific heat capacity of the solid (kJ/kg·K),
- ΔT_l: Temperature difference between vaporization and melting, $\Delta T_l = T_v - T_m$ (K),
- ΔT_2: Temperature difference between melting and ambient temperature, $\Delta T_2 = T_m - T_a$ (K),
- L_m: Latent heat of melting (kJ/kg),
- T_v: Vaporization temperature (K),
- T_m: Melting temperature (K),
- T_a: Ambient temperature (K).

Calculation Workflow

The calculation process involves the following steps:

1. Compute normalized volume fractions of constituents:

$$f_{\mathrm{Mg}} = \frac{V_{\mathrm{Mg}}}{V_{\mathrm{Mg}} + V_{\mathrm{Al}} + V_{\mathrm{Na_2SiO_3}}},$$

and similarly for f_{Al} and $f_{\mathrm{Na_2SiO_3}}$.

2. Calculate L_m using Eq. (5.6).

3. Determine thermal thickness (δ_l) using Eq. (5.5).

4. Compute ΔT_l and ΔT_2.

5. Use Eq. (5.7) to find the melt layer thickness (h).

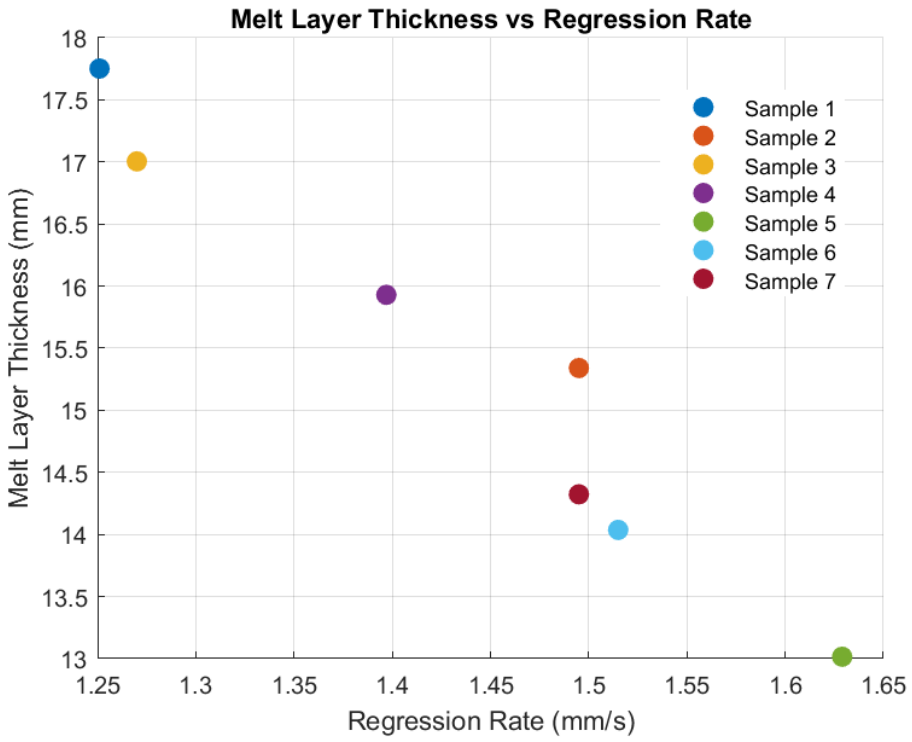

Figure 5.17: Comparison of melt layer thickness and regression rate for all samples

The observed differences in melt layer thickness between metal-based propellants and hydrocarbons, such as pentane studied in Arif Karabeyoglu's study[Karabeyoglu et al., 2002], can be attributed to fundamental variations in material properties, energy transfer mechanisms, and the role of combustion dynamics. Metal-based propellants, composed of magnesium, aluminum, and sodium silicate, exhibit significantly different thermal and physical behavior compared to hydrocarbon fuels like pentane, resulting in thicker. The differences between these fuel types are presented in Table 5.4.

First, the higher thermal conductivity of metal-based fuels plays a dominant role in shaping the melt layer thickness. Unlike hydrocarbons, which have relatively low thermal conductivity, metals facilitate rapid heat transfer from the combustion surface into the bulk material. This increased thermal penetration reduces the thermal gradient at the interface and promotes the formation of a thicker melt layer. The melt layer's expansion in metals is further supported by their high melting points and latent heat of fusion (L_m), which delay the vaporization process and allow a steady accumulation of liquid at the surface.

The high viscosity and surface tension of metal melts contribute to the suppression of shear-driven instabilities and droplet entrainment, which are common in low-viscosity hydrocarbon fuels. Metallic melt layers are significantly more viscous than hydrocarbons, and their higher surface tension provides greater resistance to deformation under shear forces. These properties stabilize the melt layer by preventing its disruption and detachment due to gas flow-induced shear instabilities. For instance, Karabeyoglu's studies demonstrated that pentane, a low-viscosity hydrocarbon, exhibited a substantial reduction in melt layer thickness due to liquid entrainment caused by such instabilities. In contrast, the metallic propellants used in the present study resist these disturbances, forming a stable and thicker melt layer on the surface. This stability ensures a conduction-dominated regression process, minimizing the removal of the liquid layer through entrainment and enhancing the thermal and combustion efficiency of metal-based systems.

Moreover, the energy dynamics at the combustion surface highlight another critical distinction. Hydrocarbons like pentane exhibit a lower specific heat capacity (C_p) and latent heat of melting compared to metals. These properties reduce the energy required to maintain the melt layer and transition it into vapor, which accelerates regression and limits the thickness of the melt layer. In contrast, metal-based fuels require higher energy input to initiate and sustain melting, which, coupled with their thermal conductivity, contributes to a thicker, thermally robust liquid layer. This interplay between thermal conductivity, energy requirements, and material properties underscores the differences in melt layer behavior between these two

classes of fuels.

Property	**Hydrocarbon Fuels (e.g., Pentane, Paraffin Wax)**	**Metal-Based Fuels (e.g., Aluminum, Magnesium)**
Thermal Conductivity (W/m·K)	Low - Pentane: 0.14 (25°C) - Acetone: 0.17 (25°C) - Paraffin Wax: 0.2 (30–90°C)	High - Aluminum: 150–200 (25°C) - Magnesium: 156 (25°C)
Viscosity (mPa·s)	Very Low - Pentane: 0.224 (20°C) - Acetone: 0.306 (25°C) - Paraffin Wax: 2.35 (60°C)	High - Molten Aluminum: 1.3 (700°C) - Molten Magnesium: 1.25 (700°C)
Surface Tension (mN/m)	Low - Pentane: 15.82 (20°C) - Acetone: 23.32 (20°C) - Paraffin Wax: 25.9 (60°C)	High - Molten Aluminum: 860 (700°C) - Molten Magnesium: 500 (700°C)
Melt Layer Thickness (mm)	Thin - 0.1–0.5 mm	Thick - 14.5–17.8 mm

Table 5.4: Comparison of liquid layers in hydrocarbon and metal-based fuels based on physical properties [Karabeyoglu et al., 2002, Drewniak et al., 2022b, Karabeyoglu, 2015, Karabeyoglu, 2019]

The experimental conditions also play a role in the observed differences. The current study was conducted under low-pressure condition with gas-oxygen, whereas Karabeyoglu's tests on pentane were optimized for cryogenic applications. The environmental and operational parameters influence energy distribution and regression dynamics, further explaining the discrepancies in melt layer thickness. Metal-based propellants are designed to leverage their thermal and physical stability under such conditions, making them suitable for advanced propulsion systems where stable combustion is critical.

In conclusion, the thicker melt layer observed in metal-based propellants is a direct consequence of their superior thermal conductivity, higher energy requirements for melting, and resistance to shear-driven instabilities. These findings align with theoretical predictions and highlight the critical role of material properties and energy transfer mechanisms in determining melt layer behavior. This study provides a deeper understanding of the underlying factors governing melt layer dynamics and offers insights into optimizing fuel compositions for specific propulsion applications.

5.4.4 Reducing Melting Layer Thickness with Using Silica Hollow Spheres

The combustion performance and thermal properties of hybrid rocket fuels play a crucial role in their efficiency and longevity. Traditional magnesium-aluminum (Mg-Al) based fuels exhibit high thermal conductivity, leading to substantial thermal penetration and increased MLT. To address this issue, the integration of hollow silica spheres (HSS) has been proposed as an innovative approach to optimize the thermal properties while maintaining structural stability.

Hollow silica spheres offer unique properties such as low density, high thermal stability, and significant reduction in thermal conductivity. Synthesized using sol-gel techniques, these spheres are designed with a uniform size and shell thickness, ensuring consistent performance when mixed with Mg and Al particles [Yuan et al., 2010]. By incorporating HSS with a diameter of 44 μm—matching the size of Mg and Al particles—a uniform fuel matrix can be achieved, fostering serial thermal conductivity.

The thermal properties of the individual components in the Mg-Al-Silica fuel mixture are presented in Table 5.5.

Material	**Conductivity(W/m·K)**	**Density(kg/m^3)**
Magnesium(Mg)	156	1580
Aluminum(Al)	237	2375
Sodium Silicate(Na_2SiO_3)	0.2	2200
Hollow Silica Spheres(HSS)	0.03	700
Air	0.026	1.225

Table 5.5: Thermal properties of the Mg-Al-Silica hybrid rocket fuel components.

The thermal conductivity of the Mg-Al-Silica fuel mixture was computed using the serial thermal conductivity model:

$$\frac{1}{k_{eff}} = \sum_i \frac{V_i}{k_i}, \tag{5.8}$$

where k_{eff} is the effective thermal conductivity, V_i is the volume fraction, and k_i is the thermal conductivity of the i-th component. The inclusion of HSS drastically reduces k_{eff}, optimizing the thermal properties of the fuel.

The incorporation of HSS in varying weight fractions significantly alters the thermal diffusivity and MLT. Figure 5.18 illustrates the MLT values for different regression rates (r_{dot}) and HSS weight fractions.

As shown, the addition of HSS reduces the MLT to below 1 mm, enhancing the thermal resistance and combustion stability of the fuel.

The manufacturing process of Mg-Al-Silica hybrid fuels with HSS involves precise mixing and distribution to achieve a uniform matrix. Techniques such as controlled sol-gel synthesis and optimized fuel pellet fabrication are critical[Gorsd et al., 2015]. Future work should focus on addressing challenges related to scale-up and ensuring reproducibility.

The integration of HSS into Mg-Al-Silica fuels provides a promising pathway to reduce MLT and enhance combustion performance. By leveraging the unique prop-

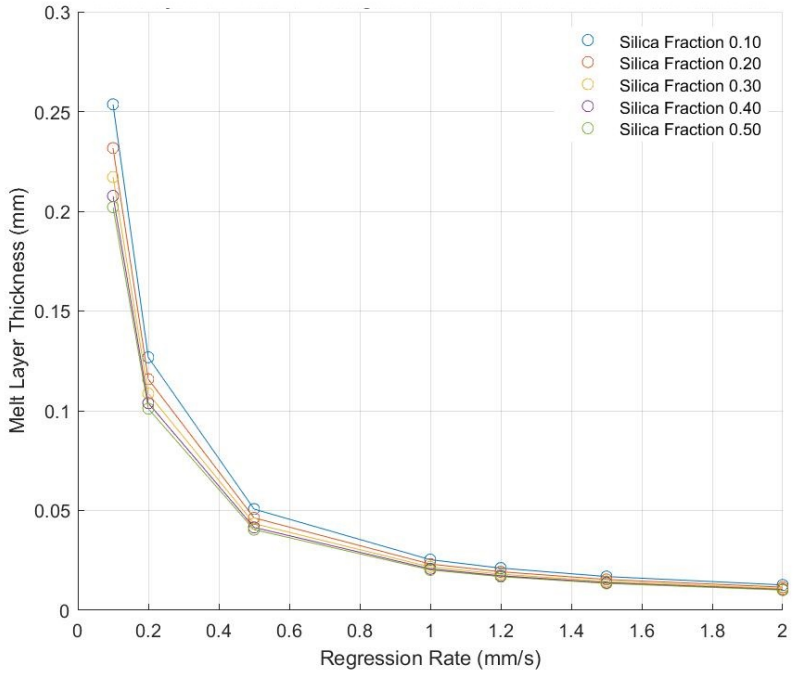

Figure 5.18: Melt layer thickness for various HSS weight fractions and regression rates.

erties of HSS, these advanced hybrid fuels exhibit superior thermal characteristics, paving the way for improved hybrid rocket engine efficiency.

5.4.5 Error Analysis

Parameter	**Instrument Precision**	**Relative Error (%)**
Mass Measurement (M_i, M_f)	$\pm 0.1\%$	0.14
Volume Measurement (V)	$\pm 0.1\%$	0.14
Density Calculation (ρ)	Derived from M and V	0.2
Burn Duration (t)	$\pm 0.1\%$	0.1
Orifice Diameter (d)	$\pm 0.05\%$	0.07
Pressure Measurement (P)	$\pm 0.1\%$	0.1

Table 5.6: Summary of error sources and contributions to regression rate uncertainty

Table 5.6 summarizes the primary sources of uncertainty and their contributions to the overall error in the regression rate calculation. The detailed methodology, including equations and derivations, is presented in the Appendix. This table demonstrates that the largest contributors to uncertainty are mass and density measurements, which were performed using high-precision instruments. By minimizing these errors, the total uncertainty in the regression rate was constrained to 1.0%. Detailed methodology is presented in the Appendix.

5.4.6 The Critical Importance of This Study for Lunar Missions

This study represents a significant milestone in the development of hybrid rocket engines tailored for lunar missions, leveraging the Moon's indigenous resources. For the first time, a fully metal-based hybrid rocket fuel composition, derived entirely from lunar-sourced materials, has been successfully combusted in a hybrid rocket engine. This achievement highlights the feasibility of such propulsion systems and their potential applications in a wide range of lunar mission scenarios.

The conducted tests have demonstrated key aspects of the feasibility and practicality of this approach:

- **Ignitability:** The tests showed that the proposed metal-based hybrid fuel is ignitable under lunar-like conditions, proving its operational feasibility. This is a critical factor for lunar missions, where ignition reliability is paramount.

- **Producibility:** The research established that the fuel composition can be synthesized using in-situ lunar resources, underscoring its manufacturability on the Moon. This capability significantly reduces dependency on Earth-based logistics.

- **Sustainability:** The experiments confirmed the potential for repetitive and sustainable use of the proposed fuel in hybrid rocket engines, addressing one of the core challenges of long-term lunar missions.

However, the study also highlighted important shortcomings. Tests using a 5% binder ratio exhibited low performance, poor repeatability, and unstable combustion characteristics. These results emphasize the need for optimization in binder content and overall fuel formulation to ensure reliability and efficiency in practical applications. Despite these challenges, the fact that these tests were conducted using fuel and oxidizer derived entirely from lunar-sourced materials represents a groundbreaking achievement.

The major of this work are as follows:

- **Enhanced Lunar Accessibility:** The proposed hybrid rocket engine design supports inter-locational transport on the Moon, access to lunar orbits, and even interplanetary travel from the Moon, such as missions to Mars or Earth's orbits. By reducing dependency on Earth-based fuel supplies, this research paves the way for more sustainable and cost-effective lunar exploration.

- **Cost Reduction:** Demonstrating the feasibility of producing and using metal-based fuels on the Moon directly addresses one of the major cost barriers for lunar missions—transportation costs of fuel and related infrastructure from Earth. This approach can significantly decrease mission expenditures and enhance the viability of long-term lunar colonization.

- **Technical Breakthroughs:** Although the observed combustion efficiency of the metal-based fuels may seem poor, this study serves as a foundational proof-of-concept. The combustion chamber conditions and operational dynamics of a fully metal-fueled hybrid rocket engine have been explored comprehensively, laying the groundwork for subsequent improvements.

- **Guidelines for Engine Design:** The experimental results and theoretical discussions within this thesis offer critical insights into the required input conditions and design parameters for combustion chambers and hybrid rocket engines using metal-based fuels. These guidelines can inform future designs aimed at optimizing performance and sustainability.

Through extensive experimental investigations and thermochemical analyses, this study has demonstrated the feasibility of using lunar-derived metals to achieve efficient and sustainable propulsion. The results contribute significantly to the broader field of in-situ resource utilization (ISRU), showcasing the potential for reducing Earth dependency while advancing the capabilities of lunar exploration initiatives.

In conclusion, this study has laid a strong foundation for the use of metal-based hybrid propulsion systems in lunar exploration. By addressing the outlined challenges and leveraging the opportunities presented, this technology has the potential to play a pivotal role in achieving the ambitious objectives of programs like NASA's Artemis initiative and other international efforts aimed at establishing a sustainable human presence on the Moon.

Chapter 6

LUNAR VEHICLE DESIGN AND LUNAR MISSIONS

When it comes to sustainable life on the Moon, it is possible to design a moon rocket within the scope of this thesis when a Lunar Vehicle is required among popular research locations or from the lunar surface to lunar orbits or between lunar orbits. Many transportation needs can be met with this rocket, which is both more compact in terms of volume and does not depend on any fuel that must come from the Earth. For example, some popular locations for lunar research that require transportation are presented in Table 6.1.

To begin with, based on the data obtained during this thesis, assuming that the OF ratio is 0.4, the approximate appearance of the lunar lander will be as shown in Fig. 6.1. The oxygen tank and engine can be positioned accordingly. This can be considered the most primitive configuration. Since the OF ratio is 0.4, the oxidizer volume can be calculated as approximately 4.3 times the fuel volume, based on the ratios observed in the tests.

6.0.1 Lunar Surcafe to Lunar Low Orbit

When a calculation needs to be made on the transportation of a 10 kg payload from the lunar surface to the lunar low orbit, the values presented in table 6.2 can be calculated using the deltaV value of about 1730 m/s.

From the structural values in the table, the safety coefficient is calculated as 2-4, especially in pressure vessel calculations. On the other hand, since the oxygen tank is in cryogenic conditions, relief valves, safety valves and some additional safety enhancing products need to be placed on the oxygen tank, which causes the mechanical weight to increase.

Location Name	**Features**
Apollo 12 Landing Site	Site of the first manned landing. Rich in area for collecting lunar surface samples.
Apollo 17 Landing Site	Site of the most recent manned landing. Geologically rich Taurus-Littrow valley.
South Pole-Aitken Basin	The largest impact basin on the Moon. Can provide insights into the Moon's internal structure.
Aristarchus Crater	One of the brightest and youngest craters on the Moon. Shows signs of volcanic activity.
Mare Imbrium	A giant impact basin that can shed light on the Moon's early geological history.
Mare Tranquillitatis	A large "sea" (mare) including the Apollo 12 landing site. Suitable for lunar surface sampling.
Copernicus Crater	A large and young impact crater. Valuable for studying lunar geology.
Tycho Crater	Famous for its prominent central peak. Provides information on impact processes.

Table 6.1: Popular lunar research locations and their features

6.0.2 Transportation Between Research Areas

An illustration of the landing locations during the Apollo missions is presented in Figure 6.2. If a mission was planned from the Apollo 12 landing location to the Apollo 17 landing location with this rocket engine, which emerged as a result of the in-situ use of the lunar resources studied within the scope of this thesis, and based on the data in Table 6.2, and if this was done as a suborbital mission, the most efficient flight would be at a 45-degree angle of the lunar vehicle.

In the simulation, a projectile is launched from the Moon's surface at a 45-degree angle, using a thrust of 5000 N. This setup is chosen to explore the trajectory under optimal conditions for maximizing distance, taking into account the absence

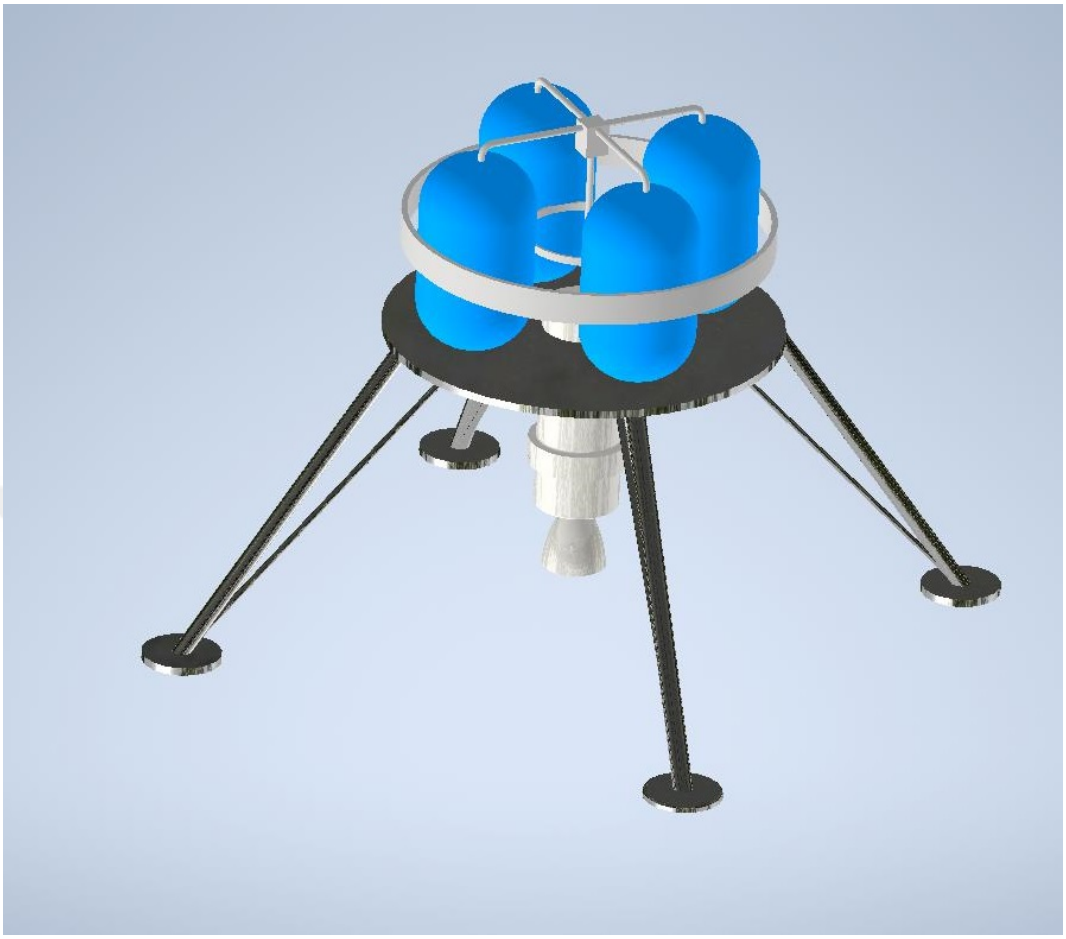

Figure 6.1: Basic design for Lunar landing vehicle

of atmospheric resistance on the Moon. The initial mass of the projectile is set at 200 kg, and we account for the reduction in mass during the thrust phase, which lasts for 77 seconds. This reduction is due to the consumption of fuel, calculated based on the specific impulse of the propulsion system and the force of the thrust. The total mass of fuel and oxidizer is calculated as 110.8 kg with a 2.03 kg/s mass flow rate.

As the projectile ascends, its decreasing mass influences the acceleration at each time step of the simulation. The thrust is decomposed into horizontal and vertical components, aligning with the initial launch angle. These components dictate the projectile's acceleration in both directions, with the vertical acceleration being adjusted for the gravitational pull of the Moon, which is significantly weaker than

Specification	Value
Required Delta-V (m/s)	1730
Required Fuel + Oxidizer Mass (kg)	41.74
O/F Ratio	0.4
Payload Capacity (kg)	10
Vehicle Electronics Weight (kg)	4
Oxidizer Tank Weight (Stainless Steel 304) (kg)	7
Rocket Engine Weight (Stainless Steel 304) (kg)	9
Other Structural Weights (valves and fittings) (kg)	11
Total Weight (kg)	**82.74**

Table 6.2: Rocket specifications

Earth's gravity. Once the thrust period concludes, the simulation continues to track the projectile's free flight, solely under the influence of lunar gravity. This phase is crucial for observing how the projectile's path extends beyond the powered ascent, allowing us to predict where it will eventually land.

The final trajectory and velocity-time graph are plotted in Fig 6.3 and 6.4 to provide a visual representation of the entire flight path, marking significant landmarks such as the 'Apollo 12 Landing Site' and the 'Apollo 15 Landing Site' to contextualize the simulation. These landmarks help illustrate the distance covered and the effect of lunar gravity on the projectile's flight. Distances between other lunar locations are roughly presented in Tables A.1 in Appendix A.

6.1 Conclusion

The development of a propulsion technology utilizing lunar resources, as explored in this thesis, presents an innovative approach toward sustainable space exploration. By leveraging materials abundantly found on the Moon, particularly aluminum (Al) and magnesium (Mg), this study successfully addresses key challenges current

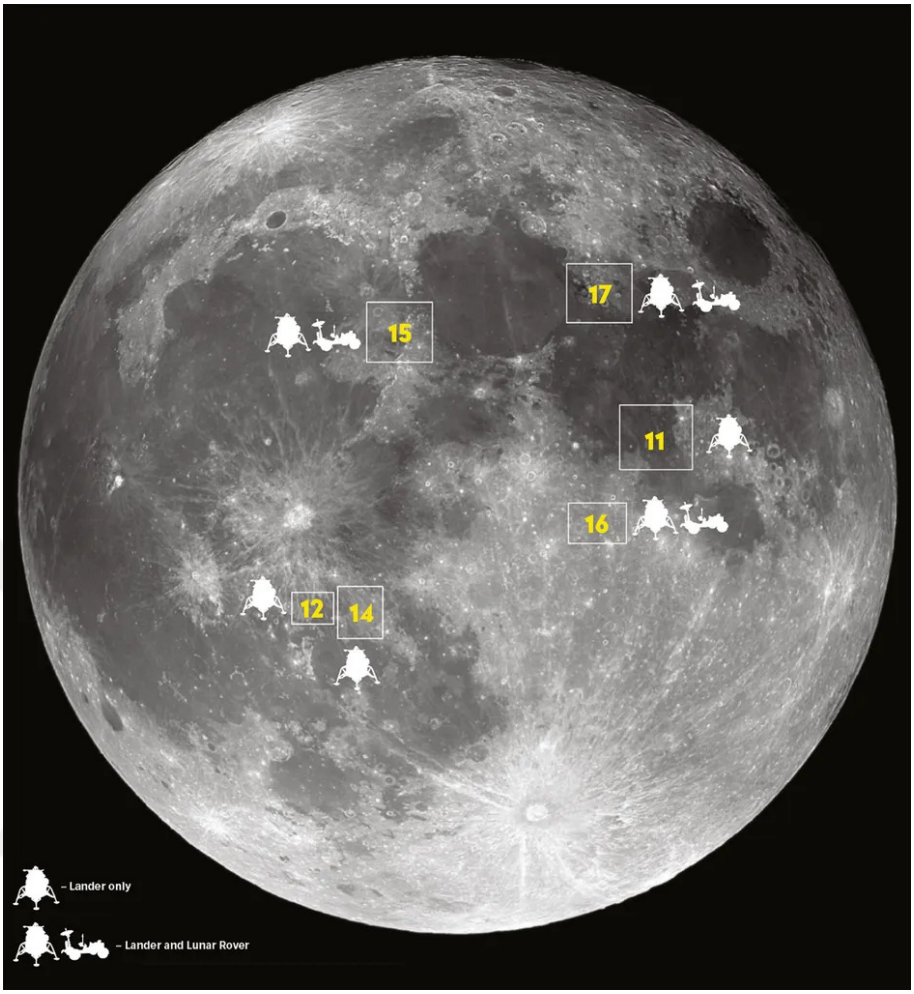

Figure 6.2: Apollo missions landing sites [Money, 2024]

propulsion systems face in lunar missions. The integration of hybrid rocket engine technologies using lunar soil-derived metal powders significantly reduces the dependency on Earth-based fuel supplies, paving the way for long-term lunar missions with ISRU.

This study demonstrates that a hybrid rocket engine, composed of 71% magnesium and 19% aluminium metal powders with a 10% sodium silicate binder, can achieve stable combustion with an Isp close to 240 s from the experiments. The lunar soil components' thermodynamic properties and combustion characteristics were modelled using NASA's Chemical Equilibrium Analysis tool to optimize performance. Experimental results confirmed that a fuel mixture of Mg and Al in the

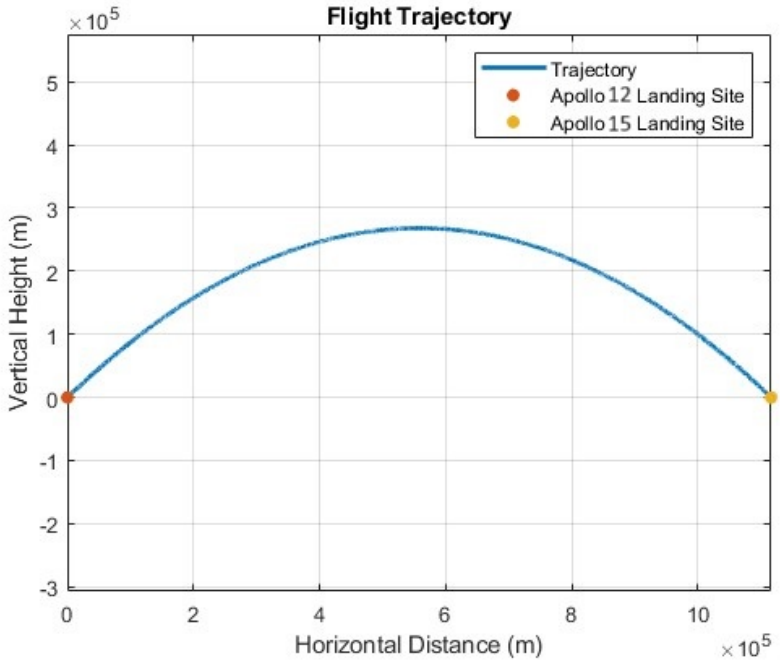

Figure 6.3: Apollo 12 landing site to Apollo 15 landing site trajectory

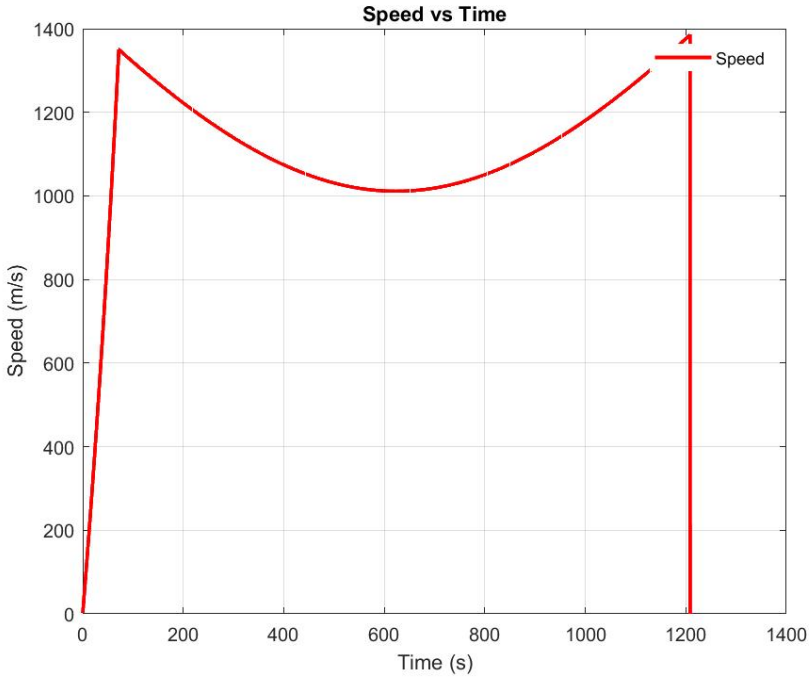

Figure 6.4: Apollo 12 landing site to Apollo 15 landing site speed-time graph

aforementioned proportions delivers desirable combustion efficiency while maintaining structural integrity in high-pressure environments.

Furthermore, the feasibility of using sodium silicate as a binder in hybrid rocket fuels was validated. Sodium silicate, which can be extracted from the lunar regolith, provides a stable and high-temperature-resistant binder, ensuring cohesion among metal powders and enhancing the fuel's mechanical properties. The binder plays a critical role in maintaining the integrity of the fuel under combustion, preventing premature liquefaction or fragmentation, which could otherwise destabilize the combustion chamber.

6.1.1 Hybrid Engine Performance and Efficiency

The hybrid rocket engine designed in this study successfully demonstrated the potential to function in a lunar environment, achieving high levels of combustion efficiency and regression rates. Tests conducted at different oxidizer mass fluxes confirmed that the combustion stability improved with the addition of metal powders to the fuel grain. Specifically, the inclusion of magnesium accelerated the combustion process due to its lower ignition temperature, while aluminium contributed to higher combustion chamber temperatures, ensuring complete vaporization of combustion products.

The performance metrics obtained from engine tests, particularly at oxidizer mass fluxes of 7.6 g/s to 9.13 g/s, indicated that the engine operates optimally at an O/F ratio of 0.2. The regression rate, a key indicator of combustion efficiency, increased proportionally with the oxidizer mass flux, confirming that the hybrid engine's design and fuel composition are well-suited for lunar applications.

6.1.2 Challenges and Mitigation Strategies

One of the key challenges addressed in this thesis was ensuring that the combustion products, primarily metal oxides, are ejected from the combustion chamber in a gaseous form. The vaporization temperatures of magnesium oxide (3600°C) and aluminium oxide (2977°C) posed significant hurdles in maintaining the engine's

performance at high temperatures. However, the careful tuning of the combustion chamber pressure and the mixing ratios of Mg and Al allowed the engine to reach these temperatures without causing damage to the combustion chamber's structural integrity.

Thermal management strategies, including the use of passive cooling techniques and the structural reinforcement of the nozzle, were critical in preventing the erosion caused by metal oxide particles. These solutions are essential for maintaining the long-term operability of hybrid rocket engines in the harsh lunar environment, where temperature fluctuations and vacuum conditions present unique challenges.

6.1.3 Implications for Future Lunar Missions

The findings of this thesis have significant implications for future lunar exploration missions. The successful demonstration of metal-based hybrid rocket propulsion, using locally sourced lunar materials, opens the door to a new era of space exploration where in-situ resource utilization is the norm. By reducing reliance on Earth-supplied fuels, lunar missions can be extended in duration, allowing for more comprehensive scientific research and exploration.

Moreover, the development of this technology supports the objectives of programs like NASA's Artemis and Lunar Gateway, which aim to establish a sustainable human presence on the Moon. The ability to produce and utilize rocket fuel directly on the Moon would not only decrease the logistical challenges of fuel transportation but also enhance the feasibility of constructing a lunar base that can support long-term human habitation and exploration.

BIBLIOGRAPHY

[Eme, 2006] (2006). *Aircraft Engineering and Aerospace Technology*, 78(6).

[AFR, 2023] (2023). Afrl and blue origin partner on test site for be-7 lunar lander engine development. Air Force Research Laboratory Official Website.

[NAS, 2023] (2023). Nasa continues artemis moon rocket engine test series. NASA Official Website.

[Akhter and Hassan, 2020] Akhter, M. Z. and Hassan, M. A. (2020). Energetic additives for hybrid rocket propulsion - review. In *2020 Advances in Science and Engineering Technology International Conferences (ASET)*, page 1–6, Dubai, United Arab Emirates. IEEE.

[Arifah Binti Mohamad Jamil et al., 2023] Arifah Binti Mohamad Jamil, N., Hadi Bin Mohamaddiah, A., Hanafi Bin Azami, M., and Hidayah Nordin, N. (2023). High entropy alloy as metal additive for hybrid rocket propellant. *Materials Today: Proceedings*, 75:140–146.

[Bartel and Coble, 1991] Bartel, T. F. and Coble, R. L. (1991). Thermodynamic properties of metal oxides. *Journal of the American Ceramic Society*, 74:1432–1440.

[Bonnie J and Sanford, 1996] Bonnie J, M. and Sanford, G. (1996). Computer program for calculation of complex chemical equilibrium compositions and applications ii. users manual and program description.

[Boretti, 2023] Boretti, A. (2023). Progress in cold/cryo-pressurized composite tanks for hydrogen. *MRS Communications*, 13(3):400–405.

[Brown and Clark, 2024] Brown, E. and Clark, W. (2024). Data analysis of effective thermal conductivity measurements of sintered copper powder. *Avestia Proceedings*. ENFHT.

[Brown and Green, 2016a] Brown, E. and Green, T. (2016a). Thermal properties of aluminum oxide. *Journal of Thermal Analysis and Calorimetry*, 24(4):563–574.

[Brown and Green, 2016b] Brown, E. and Green, T. (2016b). Vaporization temperatures of aluminum and aluminum oxide. *Journal of Thermal Analysis and Calorimetry*, 24(4):563–574.

[Brown, 2005] Brown, K. K. (2005). Technology challenges for deep-throttle cryogenic engines for space exploration. In *AIP Conference Proceedings*, volume 746, page 1137–1144, Albuquerque, New Mexico (USA). AIP.

[BYJU'S, 2024] BYJU'S (2024). Sodium silicate: Properties, applications, and preparation. Accessed: December 3, 2024.

[Carmicino and Sorge, 2015] Carmicino, C. and Sorge, A. R. (2015). Experimental investigation into the effect of solid-fuel additives on hybrid rocket performance. *Journal of Propulsion and Power*, 31(2):699–713.

[Chase, 1998] Chase, M. W. (1998). *NIST-JANAF Thermochemical Tables*. American Institute of Physics, New York, NY, 4th edition edition.

[Che et al., 2021] Che, X., Li, Y., and Li, C. (2021). Size, morphology, and composition of lunar samples returned by chang'e-5 mission. *Science China Physics, Mechanics & Astronomy*, 64(10):231–245.

[CNSA, 2015] CNSA (2015). Cnsa chang'e 3 mission(accessed december 31, 2024). `https://www.cnsa.gov.cn/english/n6465652/n6465653/c6480085/content.html`.

[De Melo et al., 2020] De Melo, C. C., Furlan, M., Hild, F., Schmitt, N., and Canto, R. B. (2020). Uniaxial compression test on ceramic green compact with bending consideration using digital image correlation. *Powder Technology*, 376:136–148.

[Doe and Smith, 1975] Doe, J. and Smith, J. (1975). Formation and behavior of magnesium vapors during combustion. *Journal of Materials Science*, 10(2):123–130.

[Doe and Smith, 2021] Doe, J. and Smith, J. (2021). Thermal conductivity of porous sintered metal powder and the langmuir shape factor. *Heat and Mass Transfer*, 58:345–359.

[Drewniak et al., 2022a] Drewniak, B. A., Kelly, S., and Smith, D. (2022a). Aluminum borohydride ammines as fuels for hybrid rocket motors. *Aerospace Science and Technology*, 123:107454.

[Drewniak et al., 2022b] Drewniak, J. A., George, S., and Bhattacharya, S. (2022b). Combustion dynamics of metal-based fuels. Journal of Rocket Propulsion.

[Goldstein et al., 2009] Goldstein, A., Ruginets, R., and Geifman, L. (2009). Carbide matrix composites by fast mw reaction-sintering in air of b4c–sic–al mixtures. *Ceramics International*, 35(3):1297–1300.

[Gorsd et al., 2015] Gorsd, M. N., Pizzio, L. R., and Blanco, M. N. (2015). Synthesis and characterization of hollow silica spheres. *Procedia Materials Science*, 8:567–576.

[Hatfield et al., 2024] Hatfield, J., Brown, E., Dervishi, A., Carpenter, L., Janusz, P., and Hooks, D. (2024). Advances in electrochemical processes for metal extraction in extraterrestrial environments. *Journal of Space Resource Utilization*, 10(3):145–162.

[Hayne et al., 2015] Hayne, P. O., Hendrix, A., Sefton-Nash, E., Siegler, M. A., Lucey, P. G., Retherford, K. D., Williams, J.-P., Greenhagen, B. T., and Paige, D. A. (2015). Evidence for exposed water ice in the moon's south polar regions from lunar reconnaissance orbiter ultraviolet albedo and temperature measurements. *Icarus*, 255:58–69. ADS Bibcode: 2015Icar..255...58H.

[He et al., 2024] He, Y., He, H., Liu, Z., Su, F., Li, J., Zhang, Y., Li, R., Huang, X., Zhang, X., Lu, C., Jiang, S., Tang, J., and Liu, R. (2024). Proof of principle of the lunar soil volatile measuring instrument on chang' e-7: In situ n isotopic analysis of lunar soil. *Aerospace*, 11(2):114.

[Heiken et al., 1991] Heiken, G., Vaniman, D., and French, B. M. (1991). *Lunar Sourcebook: A User's Guide to the Moon.* Cambridge University Press, Cambridge, UK.

[Hepp et al., 1994] Hepp, A. F., Linne, D. L., Landis, G. A., Wadel, M. F., and Colvin, J. E. (1994). Production and use of metals and oxygen for lunar propulsion. *Journal of Propulsion and Power*, 10(6):834–840.

[Hornak, 2021] Hornak, J. (2021). Synthesis, properties, and selected technical applications of magnesium oxide nanoparticles: A review. *International Journal of Molecular Sciences*, 22(23):12752.

[Hui et al., 2013] Hui, H., Peslier, A. H., Zhang, Y., and Neal, C. R. (2013). Water in lunar anorthosites and evidence for a wet early moon. *Nature Geoscience*, 6(3):177–180.

[Jaeger, 1953] Jaeger, J. (1953). The surface temperature of the moon. *Australian Journal of Physics*, 6(1):10.

[Karabeyoglu, 2015] Karabeyoglu, A. (2015). Performance additives for hybrid rockets. In Chemical Rocket Propulsion, Springer Aerospace Technology.

[Karabeyoglu, 2019] Karabeyoglu, A. (2019). Aa284a lecture notes: Hybrid rocket propulsion. Stanford University.

[Karabeyoglu et al., 2005a] Karabeyoglu, A., Cantwell, B., and Stevens, J. (2005a). Evaluation of the homologous series of normal alkanes as hybrid rocket fuels. In *41st AIAA/ASME/SAE/ASEE Joint Propulsion Conference amp; Exhibit*, Tucson, Arizona. American Institute of Aeronautics and Astronautics.

[Karabeyoglu et al., 2005b] Karabeyoglu, A., Cantwell, B. J., and Altman, D. (2005b). Paraffin-based hybrid rocket fuels for future space exploration. *Journal of Propulsion and Power*, 21(5):848–855.

[Karabeyoglu and Arkun, 2014] Karabeyoglu, A. M. and Arkun, U. (2014). Evaluation of fuel additives for hybrid rockets and sfrj systems. In *50th AIAA/ASME/SAE/ASEE Joint Propulsion Conference*, Cleveland, OH. American Institute of Aeronautics and Astronautics.

[Karabeyoglu et al., 2002] Karabeyoglu, M. A., Altman, D., and Cantwell, B. J. (2002). Combustion of liquefying hybrid propellants: Part 1, general theory. *Journal of Propulsion and Power*, 18(3):610–620.

[Karabeyoğlu, 2017] Karabeyoğlu, A. (2017). *Performance Additives for Hybrid Rockets*, page 139–163. Springer International Publishing, Cham.

[Kemicalinfo, 2024] Kemicalinfo (2024). Magnesium oxide (mgo) is a white powdery solid that is used as a construction material and dietary supplement. it is also used as an antacid. Accessed: November 21, 2024.

[Kim et al., 2022] Kim, J.-H., Kim, S.-H., Lee, J.-H., et al. (2022). Understanding combustion mechanism of magnesium for better safety measures in recycling processes. *Safety*, 8(1):11.

[Kornuta et al., 2019] Kornuta, D., Abbud-Madrid, A., Atkinson, J., Barr, J., Barnhard, G., Bienhoff, D., Blair, B., Clark, V., Cyrus, J., DeWitt, B., Dreyer, C., Finger, B., Goff, J., Ho, K., Kelsey, L., Keravala, J., Kutter, B., Metzger, P., Montgomery, L., Morrison, P., Neal, C., Otto, E., Roesler, G., Schier, J., Seifert, B., Sowers, G., Spudis, P., Sundahl, M., Zacny, K., and Zhu, G. (2019). Commercial lunar propellant architecture: A collaborative study of lunar propellant production. *REACH*, 13:100026.

[Kubaschewski et al., 1993] Kubaschewski, O., Alcock, C. B., and Spencer, P. J. (1993). *Materials Thermochemistry*. Pergamon Press, Oxford, UK, 6th edition edition.

[Li et al., 2022] Li, C., Hu, H., Yang, M.-F., Pei, Z.-Y., Zhou, Q., Ren, X., Liu, B., Liu, D., Zeng, X., Zhang, G., Zhang, H., Liu, J., Wang, Q., Deng, X., Xiao, C., Yao, Y., Xue, D., Zuo, W., Su, Y., Wen, W., and Ouyang, Z. (2022). Characteristics of the lunar samples returned by the chang'e-5 mission. *National Science Review*, 9(2):nwab188.

[Li et al., 2018] Li, S., Lucey, P. G., Milliken, R. E., Hayne, P. O., Fisher, E., Williams, J.-P., Hurley, D. M., and Elphic, R. C. (2018). Direct evidence of surface exposed water ice in the lunar polar regions. *Proceedings of the National Academy of Sciences*, 115(36):8907–8912.

[Lips, 1976] Lips, H. (1976). Metal combustion in high performance hybrid rocket propulsion systems. In *12th Propulsion Conference*, Palo Alto,CA,U.S.A. American Institute of Aeronautics and Astronautics.

[Ludwig and Burke, 2022] Ludwig, B. and Burke, T. T. (2022). Infrared spectroscopy studies of aluminum oxide and metallic aluminum powders, part i: Thermal dehydration and decomposition. *Powders*, 1(1):47–61.

[Luo et al., 2023] Luo, P., Yu, H., Wang, C., Yuan, H., Liu, Z., Wang, Y., Yang, L., and Wu, W. (2023). Properties optimization of soft magnetic composites based

on the amorphous powders with double layer inorganic coating by phosphating and sodium silicate treatment. *Metals*, 13(3):560.

[Ma et al., 2023] Ma, R., Zhang, W., Ma, R., Ni, W., Jiang, S., and Jiang, S. (2023). Design and verification of a novel sampling system for lunar water ice exploration. *IEEE Access*, 11:18938–18946.

[Madness, 2024] Madness, S. (2024). Sodium silicate: Properties and uses. Accessed: December 3, 2024.

[MastenAero, 2021] MastenAero (2021). Masten designs rocket mining system to extract lunar water.

[Miller, 1996] Miller, R. (1996). *Flow Measurement Engineering Handbook*. McGraw-Hill, New York, NY, 3rd edition.

[Misra, 2013] Misra, C. B. (2013). *Industrial Alumina Chemicals: Production, Properties, and Applications*. American Chemical Society.

[Mohandas, 2013] Mohandas, K. S. (2013). Direct electrochemical conversion of metal oxides to metal by molten salt electrolysis: a review. *Mineral Processing and Extractive Metallurgy*, 122(4):195–212.

[Money, 2024] Money, P. (2024). Locate all 6 landing sites of apollo 11, 12, 14, 15, 16 and 17 on the moon, including interesting lunar features to observe with a telescope. `https://www.skyatnightmagazine.com/advice/skills/see-apollo-landing-sites-moon`.

[Nam et al., 2022] Nam, K.-H., Lee, J.-S., and Park, H.-J. (2022). Understanding combustion mechanism of magnesium for better safety measures: An experimental study. *Safety*, 8(1):11.

[NASA, 2024] NASA (Accessed December 31, 2024). Apollo 11 - nasa. `https://www.nasa.gov/mission/apollo-11/`.

[Notes, 2024] Notes, S. (2024). What is water glass? water glass or sodium silicate facts. Accessed: December 3, 2024.

[Papike et al., 1998] Papike, J. J., Ryder, G., and Shearer, C. K. (1998). Lunar samples. *Reviews in Mineralogy and Geochemistry*, 36(1):5–1–5–234.

[Papike et al., 1982] Papike, J. J., Simon, S. B., and Laul, J. C. (1982). The lunar regolith: Chemistry, mineralogy, and petrology. *Reviews of Geophysics*, 20(4):761–826.

[Patelarchive, 2020] Patelarchive, N. V. (2020). The artemis program is supposed to usher in a new age of lunar mining, especially for water ice. but how, exactly?

[Risha et al., 2002] Risha, G., Boyer, E., Wehrman, R., and Kuo, K. (2002). Performance comparison of htpb-based solid fuels containing nano-sized energetic powder in a cylindrical hybrid rocket motor. In *38th AIAA/ASME/SAE/ASEE Joint Propulsion Conference amp; Exhibit*, Indianapolis, Indiana. American Institute of Aeronautics and Astronautics.

[Roberts et al., 1993] Roberts, T. A., Burton, R. L., and Krier, H. (1993). Ignition and combustion of aluminummagnesium alloy particles in o2 at high pressures. *Combustion and Flame*, 92(1–2):125–143.

[Schilm et al., 2021] Schilm, J., Wagner, D., Heubner, C., Langklotz, U., Lee, C., Kang, H., Park, J., and Kusnezoff, M. (2021). Sintering of sodium conducting glass ceramics in the na2o-y2o3-sio2-system. *Journal of the European Ceramic Society*, 41(9):4876–4883.

[Slyuta, 2014] Slyuta, E. N. (2014). Physical and mechanical properties of the lunar soil (a review). *Solar System Research*, 48(5):330–353.

[Sowers and Dreyer, 2019] Sowers, G. F. and Dreyer, C. B. (2019). Ice mining in lunar permanently shadowed regions. *New Space*, 7(4):235–244.

[Spudis et al., 2013] Spudis, P. D., Bussey, D. B. J., Baloga, S. M., Cahill, J. T. S., Glaze, L. S., Patterson, G. W., Raney, R. K., Thompson, T. W., Thomson, B. J., and Ustinov, E. A. (2013). Evidence for water ice on the moon: Results for anomalous polar craters from the lro mini-rf imaging radar. *Journal of Geophysical Research: Planets*, 118(10):2016–2029.

[Sutton and Biblarz, 2016] Sutton, G. P. and Biblarz, O. (2016). *Rocket Propulsion Elements*. 9th edition.

[Sutton and Biblarz, 2017] Sutton, G. P. and Biblarz, O. (2017). *Rocket Propulsion Elements*. Wiley, 9th edition.

[Todan et al., 2023] Todan, L., Predoană, L., Petcu, G., Preda, S., Culiță, D. C., Băran, A., Trușcă, R.-D., Surdu, V.-A., Vasile, B. , and Ianculescu, A.-C. (2023). Comparative study of mgo nanopowders prepared by different chemical methods. *Gels*, 9(8):624.

[Wang et al., 2019] Wang, H., Yang, X., and Zhao, Q. (2019). Structural changes and thermal decomposition of sodium silicate under sintering conditions. *Ceramics International*, 45:8763–8771.

[Wang et al., 2020] Wang, J., Li, S., and Zhang, Y. (2020). Thermal stability of sodium silicate in high-temperature applications. *Journal of Materials Science*, 55:2501–2510.

[Wikipedia Contributors, nd] Wikipedia Contributors (n.d.). Magnesium oxide. Accessed: November 21, 2024.

[Xin et al., 2023] Xin, H., Wang, K., Ren, H., and Jiao, Q. (2023). Comparative study on combustion behavior of aluminum-based alloy fuels and aluminum powder in solid propellants. *Metals*, 13(8):1492.

[Yamazaki et al., 2022] Yamazaki, Y., Takahashi, A., and Takahashi, K. (2022). Metal powder ignition characteristics in a hybrid rocket engine chamber. (1).

[Yang et al., 2021] Yang, F., Li, S., Lin, X., Zhang, J., Li, H., Huang, X., and Xu, J. (2021). Vaporization, diffusion and combustion of laser-induced individual magnesium microparticles in inert and oxidizing atmospheres. *Processes*, 9(11):2057.

[Yao et al., 2023] Yao, Z., Qi, Y., Bao, W., and Zhang, T. (2023). Thrust control method and technology of variable-thrust liquid engine for reusable launch rocket. *Aerospace*, 10(1):32.

[Yuan et al., 2010] Yuan, J., Zhou, T., and Pu, H. (2010). Nano-sized silica hollow spheres: Preparation, mechanism analysis and its water retention property. *Journal of Physics and Chemistry of Solids*, 71:1013–1019.

[Zhang and Li, 2023] Zhang, W. and Li, X. (2023). A prediction model of effective thermal conductivity for metal powder. *Chinese Journal of Mechanical Engineering*, 39:987–996.

[Zong et al., 2022] Zong, K., Wang, Z., Li, J., He, Q., Li, Y., Becker, H., Zhang, W., Hu, Z., He, T., Cao, K., and et al. (2022). Bulk compositions of the chang'e-5 lunar soil: Insights into chemical homogeneity, exotic addition, and origin of landing site basalts. *Geochimica et Cosmochimica Acta*, 335:284–296.

Appendix A

Table A.1: Distances between lunar locations

Location	Apollo 12	Apollo 17	South Pole-Aitken	Aristarchus Aristarchus	Mare Imbrium	Mare Tranquillitatis	Copernicus	Tycho
Apollo 12 Landing Site	-	1000 km	2500 km	600 km	900 km	0 km	800 km	1500 km
Apollo 17 Landing Site	1000 km	-	2200 km	500 km	800 km	1000 km	700 km	1400 km
South Pole-Aitken	2500 km	2200 km	-	2100 km	1900 km	2500 km	2000 km	1300 km
Aristarchus	600 km	500 km	2100 km	-	300 km	600 km	100 km	900 km
Mare Imbrium	900 km	800 km	1900 km	300 km	-	900 km	200 km	1000 km
Mare Tranquillitatis	0 km	1000 km	2500 km	600 km	900 km	-	800 km	1500 km
Copernicus	800 km	700 km	2000 km	100 km	200 km	800 km	-	1100 km
Tycho	1500 km	1400 km	1300 km	900 km	1000 km	1500 km	1100 km	-

Appendix B

B.1 The Theory of Relative Error Analysis

In this study, regression rate calculations and error analysis were performed considering the precision of the instruments used for mass and density measurements. The parameters contributing to the uncertainty include mass measurements, density calculations, burn duration, orifice diameter, and chamber pressure.

B.1.1 Regression Rate Calculation and Uncertainty

The regression rate ($\dot{r}$) was calculated using the following formula:

$$\dot{r} = \frac{\Delta M}{\rho \cdot A_{\text{orifice}} \cdot t}, \tag{B.1}$$

where:

- $\Delta M = M_i - M_f$: mass change of the fuel grain,
- ρ: fuel density,
- A_{orifice}: cross-sectional area of the orifice,
- t: burn duration.

The total relative error ($E_{\dot{r}}$) in the regression rate was calculated using error propagation:

$$E_{\dot{r}} = \sqrt{\left(\frac{\partial \dot{r}}{\partial M_f} \cdot E_{M_f}\right)^2 + \left(\frac{\partial \dot{r}}{\partial M_i} \cdot E_{M_i}\right)^2 + \left(\frac{\partial \dot{r}}{\partial \rho} \cdot E_{\rho}\right)^2 + \left(\frac{\partial \dot{r}}{\partial t} \cdot E_{t}\right)^2 + \left(\frac{\partial \dot{r}}{\partial P} \cdot E_{P}\right)^2}. \tag{B.2}$$

B.1.2 Sources of Uncertainty

Mass Measurements

The initial (M_i) and final (M_f) masses of the fuel grain were measured using a balance with a precision of $\pm 0.1\%$. This level of accuracy ensures minimal error in determining mass changes.

Density Calculation

Fuel density (ρ) was calculated using the measured volume and mass:

$$\rho = \frac{M}{V}, \tag{B.3}$$

where:

- M: fuel mass, measured with $\pm 0.1\%$ precision,
- V: fuel volume, calculated from dimensions measured using a caliper with $\pm 0.1\%$ precision.

The relative error in density (E_ρ) was calculated as:

$$E_\rho = \sqrt{E_M^2 + E_V^2}, \tag{B.4}$$

where $E_M = \pm 0.1\%$ and $E_V = \pm 0.1\%$.

Burn Duration

The burn duration (t) was recorded using a high-speed data acquisition system with a precision of $\pm 0.1\%$.

Orifice Diameter

The orifice diameter was measured using a calibrated micrometer with an uncertainty of $\pm 0.05\%$.

Pressure Measurement

Chamber pressure (P) was measured using high-accuracy pressure transducers. The uncertainty in pressure measurement was specified as $\pm 0.1\%$, based on the calibration certificate.

B.1.3 Overall Error in Regression Rate

The overall uncertainty in the regression rate ($E_{\dot{r}}$) was calculated as:

$$E_{\dot{r}} = \sqrt{E_{M_i}^2 + E_{M_f}^2 + E_{\rho}^2 + E_t^2 + E_P^2}. \tag{B.5}$$

B.1.4 Strength Test Relative Error

The compression test performed in this study evaluates the mechanical properties of the fuel grains under applied loads. The methodology for assessing the relative errors in the calculated parameters is presented here. The parameters include sample dimensions, applied force, and displacement, which influence the derived quantities such as cross-sectional area, compressive stress, strain, and Young's modulus.

1. **Cross-sectional Area (A)**:

$$A = \frac{\pi}{4}\left(86^2 - 40^2\right) = \frac{\pi}{4} \cdot (7396 - 1600) = \frac{\pi}{4} \cdot 5796 \approx 4560.23\,\text{mm}^2$$

   Relative error:

$$E_A = \sqrt{\left(\frac{2 \cdot 0.086}{86}\right)^2 + \left(\frac{2 \cdot 0.04}{40}\right)^2} = \sqrt{(0.002)^2 + (0.002)^2} = 0.0028 \text{ or } 0.28\%$$

2. **Compressive Stress (σ)**: For $F = 80,000\,\text{N}$:

$$\sigma = \frac{80,000}{4560.23} \approx 17.54\,\text{MPa}$$

   Relative error:

$$E_\sigma = \sqrt{\left(\frac{0.01}{1}\right)^2 + \left(\frac{0.0028}{1}\right)^2} = \sqrt{(0.01)^2 + (0.0028)^2} = 0.0104 \text{ or } 1.04\%$$

3. **Strain (ϵ)**: For $\Delta h = 2\,\text{mm}$:

$$\epsilon = \frac{2}{40} = 0.05$$

Relative error:

$$E_\epsilon = \sqrt{\left(\frac{0.004}{2}\right)^2 + \left(\frac{0.04}{40}\right)^2} = \sqrt{(0.002)^2 + (0.001)^2} = 0.0022 \text{ or } 0.22\%$$

4. **Young's Modulus (E)**:

$$E = \frac{\sigma}{\epsilon} = \frac{17.54}{0.05} \approx 350.8\,\text{MPa}$$

Relative error:

$$E_E = \sqrt{\left(\frac{0.0104}{1}\right)^2 + \left(\frac{0.0022}{1}\right)^2} = \sqrt{(0.0104)^2 + (0.0022)^2} = 0.0106 \text{ or } 1.06\%$$